Open access • Journal Article • DOI:10.2514/1.J052394

Experimental and numerical investigation of turbulence-airfoil noise reduction using wavy edges — Source link

Vincent Clair, Cyril Polacsek, T. Le Garrec, Gabriel Reboul ...+2 more authors

Published on: 22 Oct 2013 - AIAA Journal (American Institute of Aeronautics and Astronautics)

Topics: NACA airfoil, Computational aeroacoustics, Airfoil, Sound power and Wind tunnel

Experimental and numerical investigation of turbulence-airfoil noise reduction using wavy edges

V. Clair*, C. Polacsek †, T. Le Garrec † and G. Reboul †
ONERA – The French Aerospace Lab, F-92322 Châtillon, France
M.Gruber ‡, P. Joseph §
University of Southampton, ISVR, Tizard Building, Southampton, SO17 1BJ, UK

A passive leading edge treatment based on sinusoidal serrations aiming at reducing turbofan interaction noise has been recently studied in the framework of a European project (FLOCON). Turbulence-airfoil interaction mechanism is achieved using a turbulence grid located upstream of an isolated NACA airfoil tested in ISVR anechoic open jet wind tunnel. The experimental set-up with several airfoils designed and manufactured by Onera is first presented with main acoustic results, highlighting the sound power level reductions obtained for all studied flow speeds (about 3-4 dB reduction) without altering the aerodynamic performances (as shown by available measurements and RANS calculations). Experimental investigations are supplemented by numerical predictions in order to assess the acoustic performances of the serrations. The method described in the second part of the paper is based on a CAA code solving the nonlinear Euler equations applied to the disturbances, and coupled to a Ffowcs-Williams and Hawkings formulation. Convection effects are achieved from a RANS solution or approximated by a fully uniform flow. The upstream turbulence is synthesized by means of a stochastic model and injected into the computational domain through an adapted boundary condition. It is first validated in 2D and 3D against academic flat plate configurations by comparison with Amiet solutions (exact in such cases). Finally, 3D computations are applied to FLOCON configurations. The present methodology is shown to reproduce the measured spectra and far-field directivities with a reasonably good precision. Radiated sound level attenuation due to the serrations versus frequency is fairly well assessed too.

Nomenclature

a_0	Speed of sound
A_s	Amplitude of a serration
c	Airfoil chord
$g(x, k_x, k_y)$	Normalized aerodynamic response of the airfoil
$\hat{G}(\boldsymbol{x}, \omega \vert \boldsymbol{y})$	Free-field Green's function with uniform flow convection in the frequency domain
k_x, k_y	Streamwise and Spanwise wavenumbers (respectively)
$k_i^* = k_i c/2$	Wavenumber nondimensionalized by half the chord
L_{span}	Airfoil span
$M = U_0/a_0$	Mach number of the uniform mean flow U_0
$p', \overline{p}, p$	Pressure disturbance, mean pressure and total pressure (respectively)
T_I	Turbulence intensity
U_0	Uniform mean flow speed
$\boldsymbol{u'} = (u', v', w')$	Velocity disturbance vector
$\overline{\boldsymbol{u}}$	Mean velocity vector

*PhD Student, Computational Fluid Dynamics and Aeroacoustics Department.
†Research Engineer, Computational Fluid Dynamics and Aeroacoustics Department.
‡PhD Student, Institute of Sound and Vibration Reasearch.
§Professor, Institute of Sound and Vibration Reasearch.

$\boldsymbol{u} = \boldsymbol{u'} + \overline{\boldsymbol{u}}$	Total velocity vector
V_g	Speed of wave propagation
x, y, z	Streamwise, spanwise and upwash directions (respectively)
$\boldsymbol{x}$	Observer position
$\boldsymbol{y}$	Source position
α	Angle of attack
$\Delta k_x, \Delta k_y$	Streamwise and Spanwise wavenumber spacing (respectively)
γ	Lean angle
Λ	Integral length scale
λ_s	Wavelength of a serration
ρ', ρ	Density disturbance, and total density (respectively)
ρ_∞	Freestream density
Φ_{ww}	Upwash velocity spectrum
φ	Random phase

AoA	Angle of Attack
CAA	Computational Aeroacoustics
CFD	Computational Fluid Dynamics
FWH	Ffowcs-Williams and Hawkings
HIT	Homogeneous Isotropic Turbulence
RANS	Reynolds Averaged Navier-Stokes
LES	Large Eddy Simulation
PSD	Power Spectral Density
SPL	Sound Pressure Level

I. Introduction

Turbulent wakes generated by turbofan blades and interacting with the outlet guide vanes are known to be the main contributing source of broadband noise in aero-engines at approach conditions. The prediction and the reduction of broadband noise component due to turbulent sources interactions are then highly required by engine manufacturers. Turbofan rotor-stator full 3D stage is out of reach of today unsteady CFD computing capabilities. However,when analytical modeling is no longer possible, turbulent sources are generally studied through simplified configurations for which high-fidelity numerical simulations can be investigated. This was the motivation of two consecutive European projects PROBAND and FLOCON, respectively devoted to turbofan broadband noise prediction and reduction, by focusing on identified source mechanisms applied to generic cases such as rod-airfoil[1] or turbulence-airfoil[2] configurations. Passive treatments aiming at reducing turbulence interaction noise have been studied in FLOCON. A concept based on sinusoidal serrations (wavy edges) at the leading edge of a single airfoil has been investigated by Onera. Turbulence-airfoil interaction mechanism is achieved using a turbulence grid located upstream of a NACA airfoil tested in ISVR (Institute of Sound and Vibration Research) anechoic open wind tunnel. High noise reductions have been obtained for all studied flow speeds[3] and prediction methods have been investigated to try to assess these results.

Analytical approaches, such as the well-known Amiet model[4,5] can be adopted to estimate the noise generated by turbulent flows impacting thin airfoils, but they are limited by the flat-plate assumptions. The development of numerical methods allowing more complex geometries and realistic flows is required. This is mandatory for example to study the serration effects on acoustics. Gust-airfoil interaction problem has been extensively investigated in numerous publications and more recently extended to turbulent source problem by means of different stochastic models to be coupled to the CAA. Lockard and Morris[6,7] solved the gust-airfoil interaction case for NACA 0006 and NACA 0012 using a Navier-Stokes code. Scott[8] provided benchmark solutions using the linearized Euler solver GUST3D for a linear vortical gust impinging on a Joukowski airfoil. Golubev et al.[9–12] performed a vast study on the gust-airfoil interaction, taking interest on high frequencies and high amplitudes effects. Hixon et al.[13–15] also worked on this problem using the NASA code *BASS*. Thus the gust-airfoil problem was numerically solved and recently extended to a three-dimensional annular cascade. In all these studies the incoming disturbance is limited to a single harmonic. Broadband calculations have also been performed by Ewert[16] using turbulence stochastic models for slat

noise predictions. The generation of the turbulent field is obtained by filtering white noise. Dieste and Gabard[17,18] also use this kind of stochastic model to simulate the turbulent wake / flat plate interaction. Salem-Said[19] interests in the interaction between a homogeneous turbulence with a flat plate cascade using LES and a Fourier-mode decomposition of a prescribed kinetic energy spectrum to synthesize the turbulent inflow.[20–22]

In the European project FLOCON, two different numerical methods have been proposed by Onera to compute turbulence-airfoil interaction noise. Each method is aiming at simulating baseline and serrated airfoil cases and being compared to the experimental results. The first method, developed by CERFACS is based on a RANS-LES chaining.[23]Although this approach is actually the most rigorous, it raised numerical difficulties due to a laminar/turbulent transition close to the trailing edge, creating intense vortex shedding, and leading to a dominant self-noise contribution when scattering by the airfoil surface. Thus, a second method, described in the present paper, has been suggested to avoid these problems by neglecting the viscous effects. It is based on a CAA code solving the nonlinear Euler equations applied to the disturbances. In both methods the upstream turbulence is synthesized from a stochastic model and injected into the computational domain through an adapted boundary condition. Far-field noise radiation is obtained by chaining the CAA solution to a FWH (Ffowcs-Williams and Hawkings) integral, and by using the unsteady wall pressure as input data (solid surface formulation) or by taking virtual sources along a control surface surrounding the airfoil (porous surface formulation). The passive treatment and serration effects are described in section II. Section III is devoted to experimental set-up and wind tunnel tests with relevant aerodynamic and acoustic results. The CAA methodology is detailed in section IV and applied to FLOCON configurations in section V. To conclude, capability and perspectives of leading edge serrations applied to the OGV (outlet guide vanes) of a turbofan stage are discussed, and possible improvement and extension of the numerical method are addressed.

II. Leading edge serrations

II.A. Serration design

Contrary to trailing edge serrations investigated by Howe in the nineties,[24,25] with direct applications to wind turbine noise reduction,[26] and recently updated and improved by ISVR in the framework of FLOCON project,[2] much less attention has been paid to leading edge treatments, in particular for acoustic purpose. Soderman[28,29] investigated leading edge serrations (inspired from bird wings) aiming at reducing helicopter noise due to rotor-self sound sources (no interaction mechanism was involved). Watts and Fish deposited a US patent[30] about aerodynamic performances of a scalloped leading edge whose numerical results were addressed in Ref. 31, 32, by investigating the aerodynamic effects of whale flipper leading-edge rounded protuberances (also called tubercles). It was shown that tubercles act as vortex generators which could increase the lift and delay the stall. This concept was applied to wind turbine blades to improve their aerodynamic performances with possible impact on noise reduction.[33] Recently, sinusoidal wavy edges have been applied to rotor blade leading edges in order to reduce the tone noise induced by the vortex shedding near the trailing edge of a NACA 0021 airfoil,[34] or caused by blade-vortex interactions in a single rotating blade experiment.[35] From the authors knowledge, this last study is the only one related to interaction sound sources of interest, and is restricted to the tones. A similar wavy-edge concept is proposed by Onera,[3] in order to reduce the turbulence-airfoil interaction broadband noise, assuming that dominant sound sources are confined to the leading edge region. In Fig. 1 is shown a sketch with the two main adjustment parameters (wavelength, λ_s and amplitude, A_s), and a view of the CAD drawing of one Onera's wings to be manufactured and tested in the FLOCON project (see section III). Sinusoidal variations of the chord length are expected to introduce spanwise correlation loss and to filter the response to turbulent structures (turning parallel cut-on modes to oblique cut-off modes), as explained in the following sub-section.

II.B. De-correlation effects and filtering of incoming gusts

Starting from incoming turbulence characteristics and thin airfoil theory, basic mechanisms that might be considered for serration design (A_s and λ_s parameters described in section II.A) are discussed here. Firstly, the serration wavelength can be adjusted with respect to the spanwise correlation length of the incoming turbulence, l_y. This correlation scale, function of frequency, can be expressed from the integral turbulence scale, Λ, assuming a HIT (homogeneous isotropic turbulence) energy spectrum, as the Von-Karman model

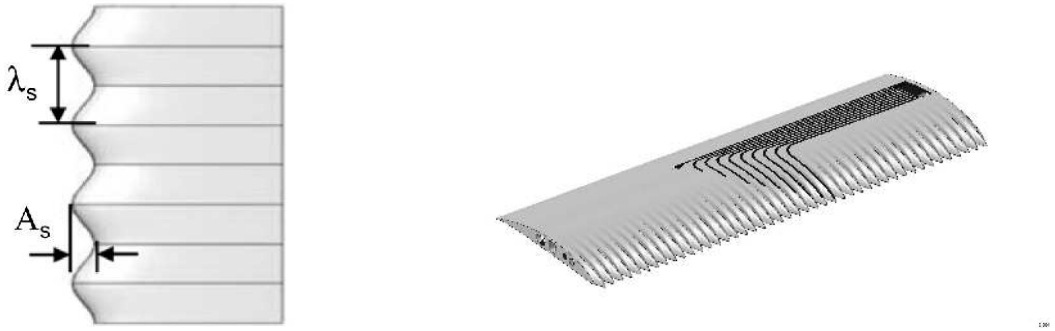

Figure 1. Wavy-edge treatment: serration parameters (left) and CAD drawing (right).

usually adopted. Typical spanwise correlation length scales with $\Lambda = 6$ mm are plotted in Fig. 2, for two convection speeds. These spectra are related to FLOCON project, for which an integral length scale of 6 mm was estimated from hot wire measurements performed in ISVR anechoic wind tunnel tests (see section III.A). Practically, this scale could be also provided by a RANS calculation applied to the present turbulence-airfoil problem (FLOCON configuration), or to a rotor-stator stage computation in the case of realistic turbofan configuration. De-correlation effects might be noticeable if chord variation between two point-sources is large enough and if the distance between these point-sources is lower than l_y. Thus, the serration half-wavelength, $\lambda_s/2$, is preferably chosen to fit the maximum value of the correlation scale l_y (almost equal to Λ). Similar approach was also adopted for trailing edge serrations in ref. [2]. Of course, the phase shifts along the leading edge are linked to the amplitude of the serration and to the frequency of the incoming perturbations, and cannot be obtained from Amiet theory (valid for straight edges). So, it seems almost impossible to assess (analytically) the acoustic performance of such effect, requiring a generalization of thin airfoil theory to the case of wavy leading edges. Extensive experimental or numerical parametrical studies (scanning Λ and λ_s values) would be helpful to draw some reliable trends.

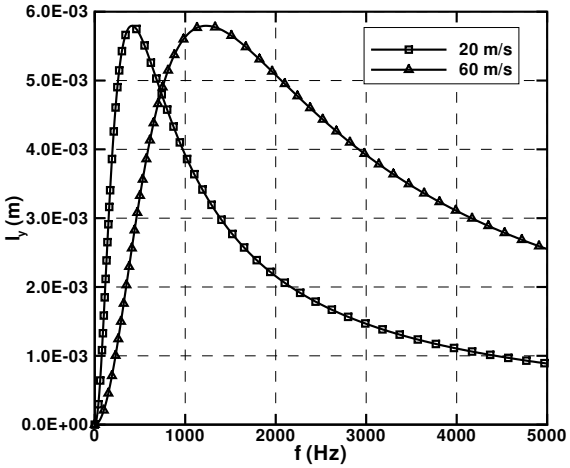

Figure 2. Spanwise correlation scale deduced from Von-Karman spectrum model (with $\Lambda = 6$ mm).

The adjustment of the serration amplitude A_s is quite challenging too. It seems right to think that A_s should be as large as possible to expect higher effects with respect to local chord and lean angle changes. However, the amplitude range has to be limited by aerodynamic constraints, since modifications of the stream flow might generate vortex shedding that could alter the aerodynamic performances. Practically, the aerodynamic behaviour is probably a priority constraint in the design process. Anyway, a second mechanism (probably involved in airfoil self-noise reduction using trailing edge serrations too) could be a modification of

aerodynamic response of the airfoil with respect to the direction of incoming perturbations (i.e., aerodynamic wave number). The serration might act as a wave-number filtering, firstly impacting the parallel gusts known to be mainly contributing to the noise radiation. To better understand this mechanism, the response of a flat plate to an oblique gust is first pointed out. It can be solved analytically, underlining a dispersion relation[36] depending on the streamwise wavenumber, k_x, the spanwise wavenumber, k_y, and the mean flow Mach number. When an oblique gust satisfies the relation $|k_y^*| < |k_x^*|M/\sqrt{1-M^2}$ (where the superscript * denotes the nondimensionalization by half the chord), the gust is called supercritical and the resulting acoustic mode is cut-on. Otherwise, the gust is called subcritical and the mode is evanescent in the case of an infinite span. This effect is illustrated in Fig. 3, in which snapshots of pressure fluctuations (issued from numerical computations) are presented for a supercritical gust (left) and a subcritical one (right). The subcritical case shows that the wall-pressure disturbances are much less intense than for the supercritical case and that the radiated (cut-off) pressure fluctuations remain confined to the vicinity of the plate.

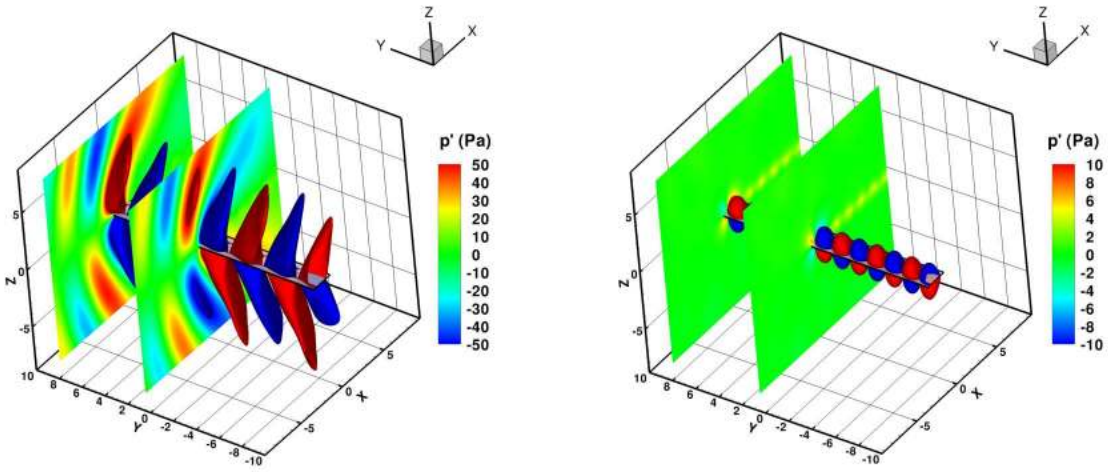

Figure 3. Snapshots of pressure fluctuations for supercritical (left) and subcritical (right) gusts.

As already discussed in Ref. [3], a simplified modeling of the leading edge serrations can be suggested by approximating the sinusoidal geometry by triangular waves (saw tooth serrations, Fig. 4). Thus, it is possible to introduce a lean angle, γ, and to extend the previous dispersion relations in performing a variable change including the leading edge position variation along the span when doing the Reissner transformation.[36] Note that the present analytical model only focuses on the spanwise variation of the chord without changing the direction of the local flow. This is different to the approach proposed by Adamczyk[37] solving the problem of an infinite swept blade with constant chord and for which the convection velocity is inclined with respect to the chordwise direction (whereas it is aligned here). The dispersion relation in our case can be rewritten and the cut-on modes are defined by $|k_{y,\gamma}^*| < |k_x^*|M/\sqrt{1-M^2}$ with $k_{y,\gamma}^*$ the modified spanwise wavenumber given by:

$$k_{y,\gamma}^* = \frac{k_x^* M^2}{1-M^2}\tan\gamma + k_y^* \tag{1}$$

The standard dispersion relation is recovered by setting $\gamma = 0°$ in Eq. (1). Solutions of the modified dispersion relation can be easily obtained, allowing us to draw the spatial filtering of the gusts for a specified lean angle, as done in Fig. 5. For the baseline case, the region of cut-on gusts is centered on the parallel modes ($k_y^* = 0$), but there are more and more cut-on oblique modes as the streamwise wavenumber (i.e. the frequency) is increasing. For high values of γ (chosen close to 90° to well distinguish the cut-on zones), this representation shows that the parallel modes (mostly contributing to the acoustic energy) are getting cut-off and that oblique modes previously cut-off by the baseline case are now cut-on. In other words, there is a spatial re-distribution from parallel to oblique gusts that is expected to provide significant noise reduction since main acoustic energy created from turbulence-airfoil mechanism is theoretically attributed to parallel modes. These arguments have to be related to experimental and numerical comparisons between baseline and serrated airfoils presented and discussed in section V.

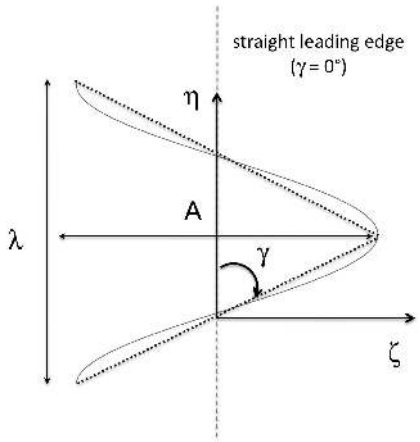

Figure 4. Sketch of triangular wave geometry.

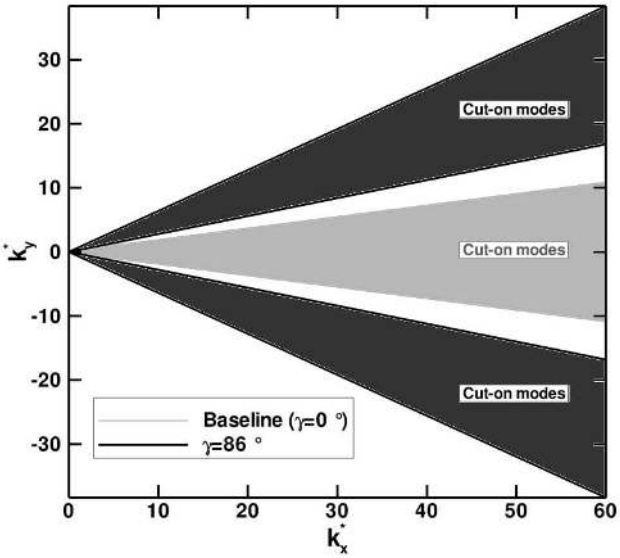

Figure 5. Filtering of the oblique gusts regarding to the lean angle.

III. Experimental investigation

III.A. Wind tunnel test description

Turbulence-airfoil mechanism has been simulated and tested in the ISVR anechoic wind tunnel.[3,27] Sound radiation measured for serrated airfoils is compared to the baseline case at several flow speeds (U_0 = 20, 40, 60 m/s) and for different AoA (angles of attack) denoted α (α = 0°, 5°, 10°, 15°). Experimental set-up is presented in Fig. 6, showing the circular antenna (located at 1.2 m from the airfoil) used to get the far-field PSD (Power Spectral Density) and directivities. A square-rods turbulence grid (Fig. 7) located inside the nozzle near the exit provides an HIT outflow whose characteristics are deduced from hot wire measurements and by comparison to a conventional von Karman spectrum model. The 1-wave number (k_x) von Karman spectrum was shown to fit very well the turbulent velocity spectra (axial component) issued from hot wire measurements for all flow speeds[27] when turbulence parameters (intensity and integral length scale) were respectively set to $TI = 2.5$ % and $\Lambda = 6$ mm as presented in Fig. 8. This set-up is appropriate for creating a dominant interaction noise contribution, as shown in Fig. 9 by comparing to measurements performed without grid (where the airfoil self noise is supposed to dominate). The airfoils have a 0.15 m chord and a 0.45 m span. The baseline airfoil geometry is detailed in Fig. 10 (left), and a picture of one ONERAs serrated wings is shown in Fig. 10 (right). Pressure tabs were implemented on airfoil surface in order to get the static pressure distributions. When possible, a tripping band made of rough sand paper is attached on the airfoil surface at 10 % of the chord, in order to trigger a turbulent transition. A set of three treated wings have been manufactured and tested:

- $\lambda_s = 6$ mm and $A_s = 10$ mm (referred as 1S)
- $\lambda_s = 10$ mm and $A_s = 10$ mm (referred as 2S)
- $\lambda_s = 10$ mm and $A_s = 15$ mm (referred as 3S)

III.B. Aerodynamic characteristics

As shown by Moreau et al.,[38] the nozzle exit flow has to be fully included in the RANS simulation to match open jet wind tunnel conditions. RANS computations with *elsA* Onera code have been performed

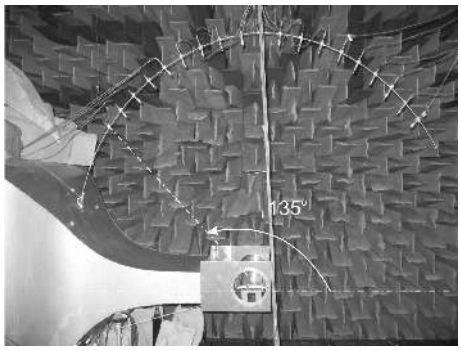

Figure 6. Experimental set-up in ISVR rig.

Figure 7. View of the turbulence grid.

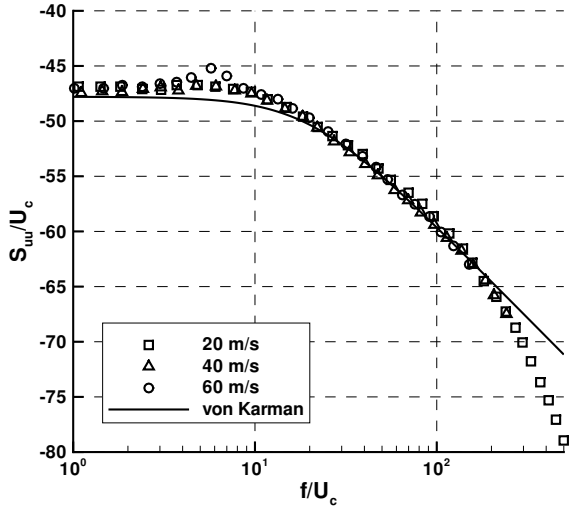

Figure 8. Comparison between the measured axial velocity spectra and the von Karman model.

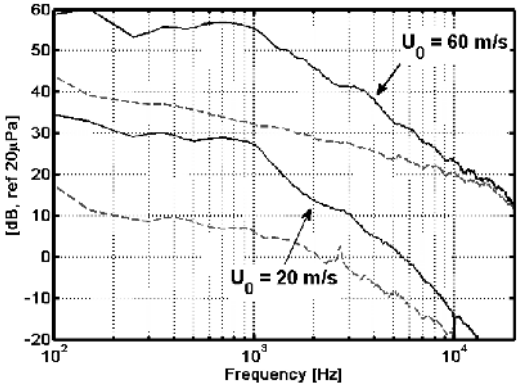

Figure 9. Interaction (full) and self-noise (dashed) measured spectra.

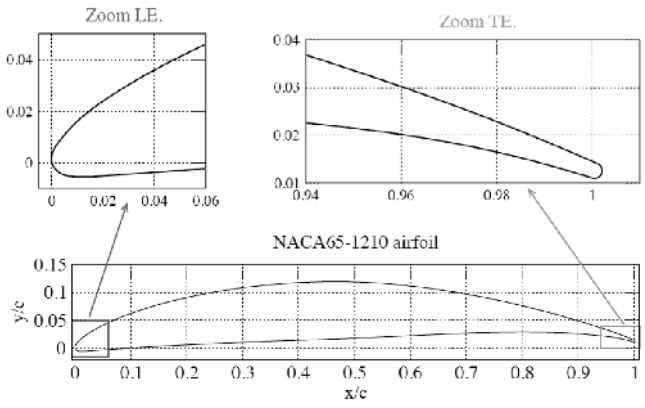

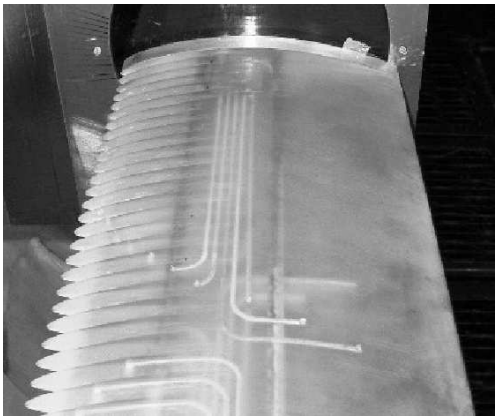

Figure 10. NACA651210 airfoil geometry (left) and ONERA serrated wing (right).

by CERFACS[23] to assess relevant aerodynamic characteristics of isolated airfoils tested in the ISVR rig. A fully turbulent $k-\omega$ SST model (with no wall transition modeling) has been adopted and a time averaging

of an unsteady RANS calculation was actually required to capture an oscillating flow separation revealed on pressure side close to the leading edge.[23] As displayed in Fig. 11, a very good agreement between predictions and tripped airfoil measurements is obtained when jet flow is taken into account. Comparisons of C_p distributions measured at ISVR on reference 0S (no serrations, no tripping) and 2S wing (using sensors located on top of the waves) are shown in Fig. 12 for the same AoA values. No tripping was used for these comparisons, because it was unpractical to attach a tripping band along the waves of ONERA serrated airfoils. However, it was assumed that the serrations should trigger a turbulent boundary layer (similarly as the tripping). Noticeable differences are visible at the leading edge region. Away, distributions are almost similar. Consequently, integration of the C_p for serrated case lead to an important increase of the lift. Similar trends have been obtained for other configurations. However, this positive effect in terms of aerodynamic performance should be pondered because pressure tabs were implemented at the top of the waves, whereas measurements at the root would probably not display the same behaviour.

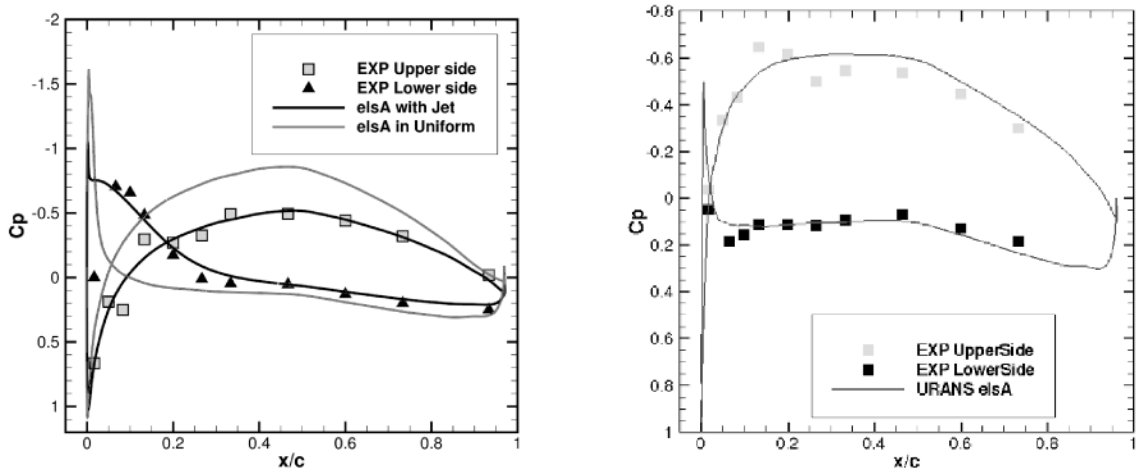

Figure 11. RANS and measured C_p distributions at $\alpha = 0°$ (left) and $10°$ (right).

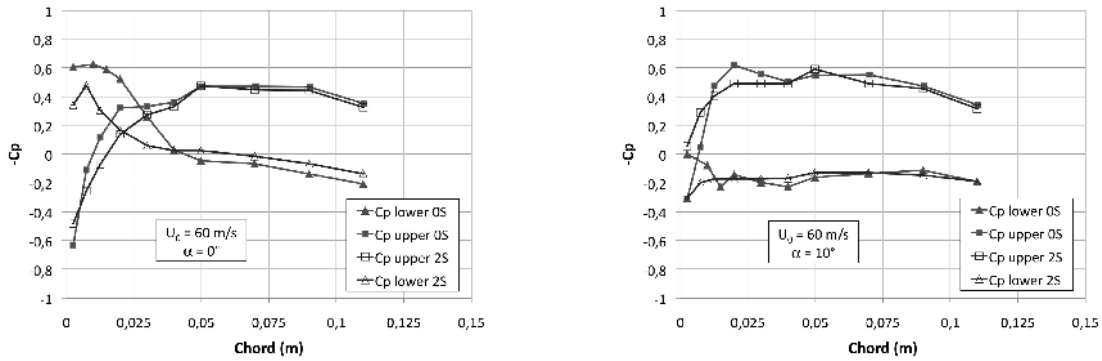

Figure 12. C_p distributions for baseline and 2S wings measured at $\alpha = 0°$ (left) and $10°$ (right).

To check this point, RANS computations have been performed on 2S wing assuming a uniform incoming mean flow (jet flow discarded), which is reasonable for estimating the relative effect of the serrations. Iso-velocity contour maps issued from 2D RANS (baseline case) and 3D RANS (serrated case) computations are presented in Fig. 13. The baseline and serrated solutions are very close, tending to show that the treatment effect on mean velocity is very low. Computed C_p at three positions (top, mid, and bottom) of a serration motif are plotted in Fig. 14. Away from leading edge region, C_p distributions are found to be almost identical, according to the measurements. Moreover, the bottom wave solution is almost identical

to the baseline solution (uniform flow) shown in Fig. 11 (left). Thus, present aerodynamic performances obtained by averaging over the span were found to be unaltered by the serrations. It is important to say that leading edge serrations are practically devoted to stator vanes (for turbofan applications) and that aerodynamic penalties are much less limiting than for a rotor blade. For an OGV, the main constraint should be to guaranty that the serrations do not alter the averaged mean flow and static pressure (as shown in Figs 13 and 14), and essentially provide the same downstream flow angle.

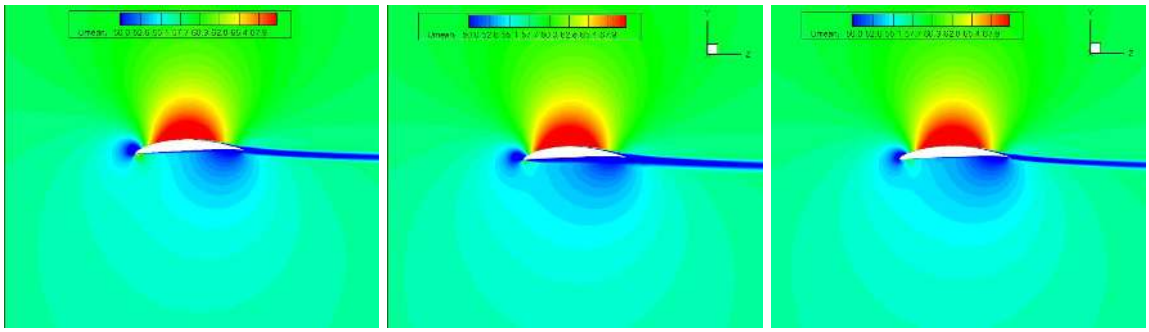

Figure 13. Spanwise slices of RANS mean velocity field around baseline and 2S wings: Baseline 0S wing (left) , bottom wave (middle) and top wave (right) of 2S wing.

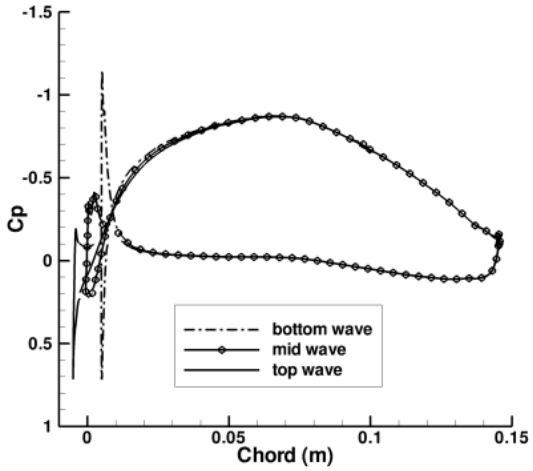

Figure 14. 3D RANS computed C_p distributions ($U_0 = 60$ m/s, $\alpha = 0°$).

III.C. Acoustic performances

The acoustic measurements carried out by ISVR have been first compared to analytical predictions based on Amiet's theory[4,5] for the baseline case (without serrations). Such comparisons are helpful to check the reliability of the radiated noise with respect to turbulence-airfoil interaction mechanism (for which Amiet's solution is theoretically exact for a flat plate in a fully uniform flow). Spectra and OASPL directivity patterns issued from Amiet's model and experiments are compared in Fig. 15 and 16, respectively. A fairly good agreement is obtained, particularly at lowest speed for which a slope correction was applied on the von Karman spectrum to better fit the hot wire measurements.[39] This simple correction currently used[39] consists in applying an exponential attenuation of the von Karman spectrum in the high frequency range (also known as von Karman-Pao spectrum) by adding a suited wave number related to the Kolmogorov scale. However, acoustic PSD were found to be unaffected by this correction at higher flow speeds (40 m/s and 60 m/s). At moderate speeds (40 m/s, 60 m/s), the peak level at low frequency and the slope of level decrease

versus frequency are slightly under-predicted by the theory. Note that low-frequency hump present in the experiment particularly visible at high speed (60 m/s) is partly due to open jet noise and installation effects as discussed in refs [2] and [27]. This mainly explains the lower predicted levels below 1 kHz. The predicted and measured directivity patterns are very close too, which makes these acoustic data quite confident for the purpose of the study.

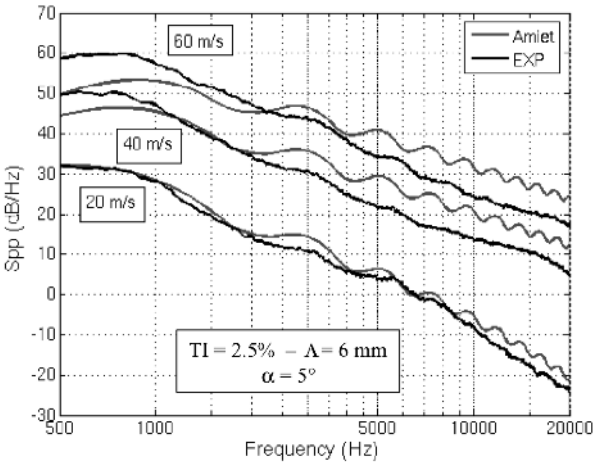

Figure 15. Predicted and measured PSD at 90°.

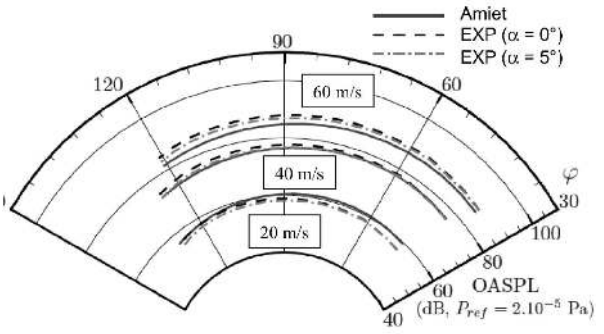

Figure 16. Predicted and measured directivities.

Next analyses are devoted to the serration effects. PSD measured at 90° for the three treatments are compared to the baseline case in Fig. 17 ($\alpha = 5°$), showing high noise reduction for a wide frequency range, more particularly at low speed. Serration effect seems to behave like a low-pass filter as the speed is increased, so that the treatments are actually efficient beyond 1 kHz at highest speed (60 m/s). A slightly better performance is obtained with treatment 3S (with largest serration amplitude). Fig. 18 summarizes the noise level reductions obtained with treatment 3S, when integrating the spectra in the range [300 Hz - 20 kHz]. It shows that good acoustic performances are reached for all AoA values (up to 15°). Fig. 19 (left) compares PSD between wing 3S and baseline, highlighting large noise reductions in the mid-frequency range (about 6 dB at 3 kHz). OASPL directivity related to microphone antenna and calculated by integrating the spectra from 1 kHz is shown in Fig. 19 (right). Acoustic performances appear to be slightly lowered in the front arc (2.2 dB reduction) compared to the rear one (3 dB reduction). The numerical assessment of acoustic results obtained from ISVR tests is now discussed in the next sections.

IV. Computational method and numerical predictions

IV.A. CAA solver and boundary conditions

The current calculations are performed with the ONERA code *sAbrinA.v0* developed by Redonnet.[40–42] It solves the full Euler equations in the time domain, and applying a perturbation form that consists in a splitting of the conservative variables into a mean flow and a fluctuating field. These equations are cast in generalized curvilinear coordinates to simulate flows around complex bodies. Such methodology is classically conducted with the help of low-dissipative high-order finite differences (6^{th} order spatial derivatives and 10^{th} order filters), and a 3^{rd} order Runge-Kutta time marching scheme. The code features multi-block structured grids and is parallelized using the MPI library.

To perform rotor-stator interaction CAA calculations, efficient numerical boundary conditions are required to allow hydrodynamic perturbations to be imposed at the inflow boundary and both hydrodynamic and acoustic outgoing waves to leave the domain without reflections. For this purpose, Tam and al.[43] derived boundary conditions from the asymptotic solutions of the linearized Euler equations. The outflow boundary

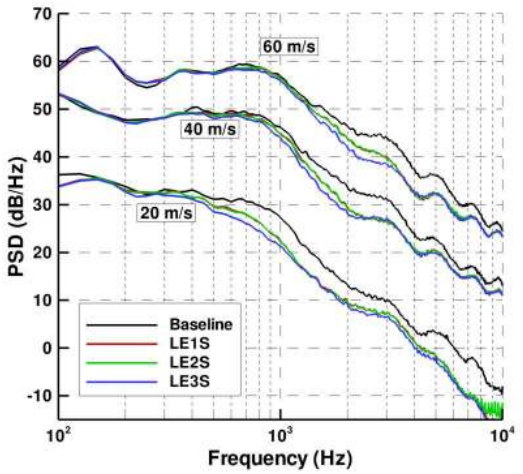

Figure 17. Baseline and serrated wing spectra at 90°.

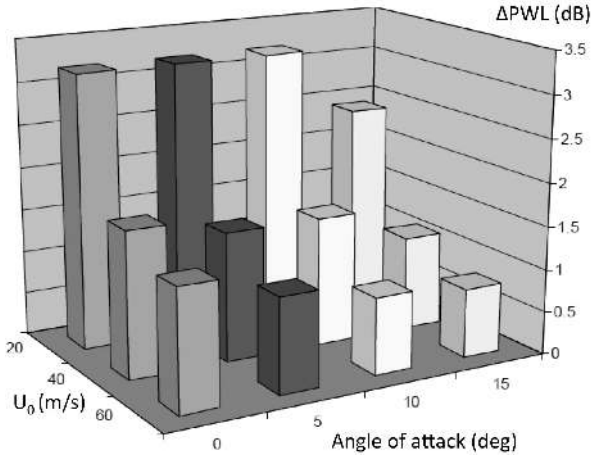

Figure 18. PWL reductions using 3S wing.

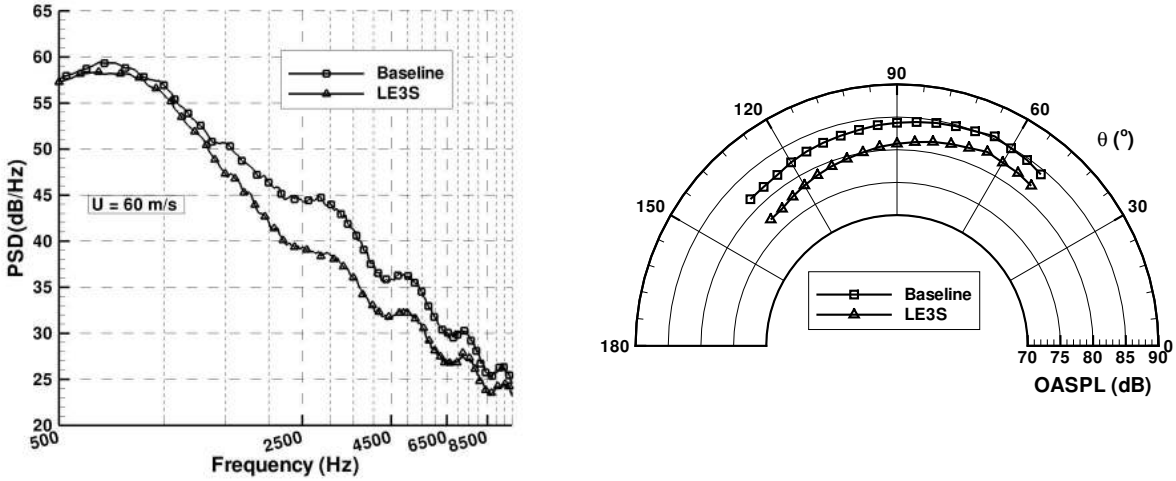

Figure 19. Baseline-3S comparisons of PSD (left) and OASPL directivities (right) at 60 m/s.

condition is written:

$$\begin{aligned}
&\frac{\partial \rho'}{\partial t} + \overline{\boldsymbol{u}}.\nabla\rho' = \frac{1}{{a_0}^2}\left(\frac{\partial p'}{\partial t} + \overline{\boldsymbol{u}}.\nabla p'\right)\\
&\frac{\partial \boldsymbol{u'}}{\partial t} + \overline{\boldsymbol{u}}.\nabla\boldsymbol{u'} = \frac{-1}{\overline{\rho}}\nabla p'\\
&\frac{1}{V_g}\frac{\partial p'}{\partial t} + \frac{\partial p'}{\partial r} + \frac{p'}{r} = 0
\end{aligned} \tag{2}$$

where $V_g = \overline{\mathbf{u}}.\mathbf{e_r} + \sqrt{{a_0}^2 - (\overline{\mathbf{u}}.\mathbf{e_\theta})^2 - (\overline{\mathbf{u}}.\mathbf{e_\phi})^2}$ is the speed of wave propagation in spherical coordinates. This condition was tested on basic cases and was found to be very efficient without the need of using stretched cells near the outflow boundaries. The incoming perturbations are injected in the computational domain

through the inflow boundary using Tam's inflow condition:

$$\left(\frac{1}{V_g}\frac{\partial}{\partial t}+\frac{\partial}{\partial r}+\frac{1}{r}\right)\begin{pmatrix}\rho'\\ \boldsymbol{u'}\\ p'\end{pmatrix}=\left(\frac{1}{V_g}\frac{\partial}{\partial t}+\frac{\partial}{\partial r}+\frac{1}{r}\right)\begin{pmatrix}\rho'_i\\ \boldsymbol{u'_i}\\ p'_i\end{pmatrix} \tag{3}$$

where the subscript "i" denotes the incoming perturbation variables. This boundary condition allows simultaneously the injection of the incoming perturbations and the exit of outgoing acoustics waves. Tam[44] argues that an improvement in the numerical accuracy can be found by using, if it is known, the exact expression of the derivatives in the right side of Eq. (3) instead of letting them be calculated by the numerical scheme. The *sAbrinA.v0* solver uses a range of ghost-point rows generated automatically around the physical domains to perform the MPI exchanges required to ensure the continuity between the split domains. These ghost-points are also used for boundary conditions purposes. Tam's boundary conditions are calculated in these points only, and the spatial derivatives needed in the boundary conditions are calculated using standard uncentered finite difference schemes.

Tam's boundary conditions are generally written in spherical coordinates, and a point in the computational domain is judiciously chosen to be the radiation centre. However, for airfoil calculations over a long span with periodicity conditions in the spanwise direction, a more suited cylindrical formulation can be adopted. The radiation centre is translated along the span when calculating the radius and the radial derivative in a cylindrical coordinates system (r, y, θ) instead of a spherical one in Eq. (2) and (3). Fig. 20 represents a snapshot of the pressure fluctuation for a 3D gust-airfoil test case using the spherical (left) and cylindrical (right) formulations of the boundary conditions. This case was only designed to highlight the benefits of the cylindrical formulation but not to perform an accurate calculation. A coarse mesh therefore has been used to permit a fast computation. In Fig. 20 (left), one can observe that for the slices far from the mid-span plane the wavefronts are deformed, whereas in Fig. 20 (right), the patterns are perfectly reproduced along the span (as expected for this case).

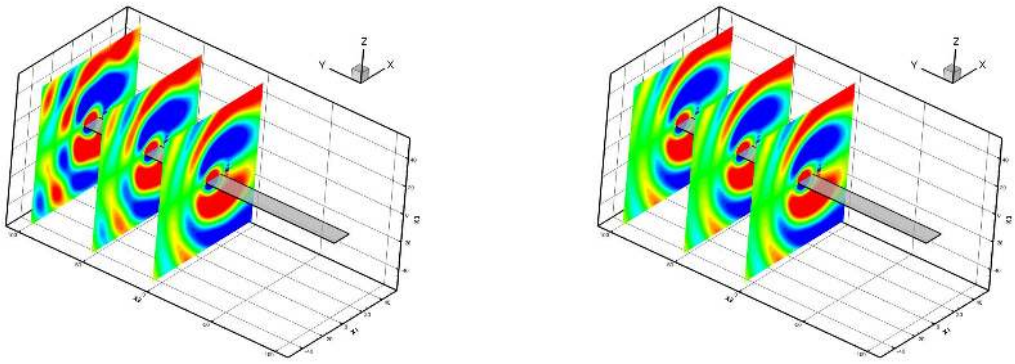

Figure 20. Pressure fluctuation snapshots of a gust-airfoil test case: Tam's boundary conditions using spherical formulation (left) or cylindrical formulation (right).

IV.B. Stochastic model of the prescribed turbulent field

The stochastic model presented here is inspired from Kraichnan's theory.[45] As done in ref. [19], it is based on a Fourier-modes decomposition of the incoming turbulent wake modeled as homogeneous isotropic turbulence (HIT) energy spectrum. In the present study, only the upwash velocity component (normal to the airfoil assimilated as a flat plate) is considered with a spatial distribution over streamwise and spanwise wavenumbers, as done in Amiet's theory[4,5] (Fig. 21). This restriction will be discussed in section IV.D.

The modes amplitudes are fitted by a von Karman energy spectrum, defined by two parameters: the turbulence intensity, T_I, and the integral lengthscale, Λ. Following the approach of Casper and Farassat,[46] 3D calculations are performed using a two-wavenumber spectrum $\Phi_{ww}(k_x, k_y)$ corresponding to the integration of the three-dimensional energy spectrum over the normal wavenumber (k_z). In the same way, for 2D calculations, the spectrum is integrated over the spanwise wavenumber (k_y) to obtain the unidimensional

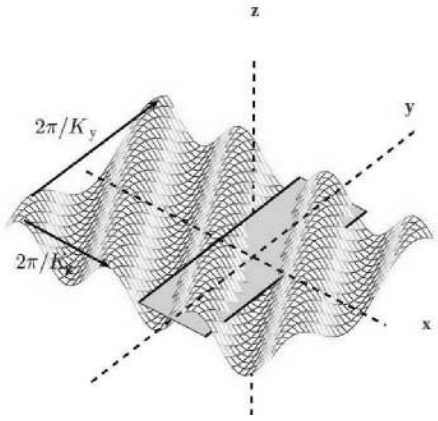

Figure 21. Coordinates system used for the turbulence-airfoil interaction model.

spectrum, $\Phi_{ww}(k_x)$ as used in ref. [17]. Thus, the incoming velocity field can be written as:

$$u'(\boldsymbol{x},t) = v'(\boldsymbol{x},t) = 0$$

$$w'(\boldsymbol{x},t) = \sum_{i=1}^{N}\sum_{j=-M}^{M} 2\sqrt{\Phi_{ww}(k_{x,i},k_{y,j})\Delta k_x \Delta k_y}\cos(k_{x,i}x + k_{y,j}y - \omega_i t + \varphi_{ij}) \qquad [3D] \tag{4}$$

$$w'(\boldsymbol{x},t) = \sum_{i=1}^{N} 2\sqrt{\Phi_{ww}(k_{x,i})\Delta k_x}\cos(k_{x,i}x - \omega_i t + \varphi_i) \qquad [2D] \tag{5}$$

The unsteady disturbance field is assumed to be convected through a uniform mean flow U_0 in the x direction (Taylor's frozen turbulence hypothesis), so that the angular frequency ω_i is related to the streamwise wavenumber by $\omega_i = U_0 k_{x,i}$. $\varphi_{i,j}$ is a random phase associated to the (i,j) mode, chosen between 0 and 2π. When considering a realistic RANS mean flow in the CAA, the convection speed of the frozen turbulence in set equal to the undisturbed upstream flow. The synthetic turbulent field so obtained is divergence-free, which prevents from creating any additional sound sources. The accuracy of the present methodology and ability of injecting this synthetic turbulence field in the CAA without introducing any dissipation and numerical reflections will be demonstrated in section IV.D devoted to academic validation cases.

IV.C. Far-field radiation

Although the acoustic response of the airfoil can be directly provided by the Euler computation if the domain is large enough to reach the far-field, the acoustic radiation can be practically obtained by integral methods (Kirchhoff or Ffowcs-Williams and Hawkings formulations) allowing us to limit the size of the mesh. This is of particular interest for 3D cases with complex geometries. Turbulence-airfoil interaction mechanism is known to create dipole sources distributed over the airfoil surface. Thus, in the following 3D computations, far-field radiation can be calculated using a standard (solid surface) FWH method, restricted to the loading noise term as in Curle's[47] theory. A frequency domain approach is adopted here, which can be written:

$$\hat{p}(\boldsymbol{x},\omega) = \int_S \hat{p}(\boldsymbol{y},\omega) n_i . \frac{\partial \hat{G}(\boldsymbol{x},\omega|\boldsymbol{y})}{\partial y_i} dS \tag{6}$$

where $\boldsymbol{x}$ is the observation position and $\boldsymbol{y}$ is the source position. $\hat{G}(\boldsymbol{x},\omega|\boldsymbol{y})$ is the free field Green's function with uniform flow convection, and $\hat{p}(\boldsymbol{y},\omega)$ is the Fourier transform of the unsteady wall pressure provided by *sAbrinA.v0*.

When using a realistic mean flow as in section **??**, the flow in the vicinity of the airfoil is not uniform, and the use of the free-field Green's function with uniform flow convection is biased. In order to investigate the effect on the acoustic propagation when using a realistic mean flow, a complete FWH integration on a

porous surface located far enough around the airfoil to almost match the uniform flow condition will also be performed. The FWH formulation used in the frequency domain is the following[48,49] :

$$\hat{p}(\boldsymbol{x},\omega) = \int_S i\omega \hat{Q}_n(\boldsymbol{y},\omega)\hat{G}(\boldsymbol{x},\omega|\boldsymbol{y})dS + \int_S \hat{F}_i(\boldsymbol{y},\omega)\frac{\partial \hat{G}(\boldsymbol{x},\omega|\boldsymbol{y})}{\partial y_i}dS + \int_V T_{ij}(\boldsymbol{y},\omega)\frac{\partial^2 \hat{G}(\boldsymbol{x},\omega|\boldsymbol{y})}{\partial y_i \partial y_j}dV \quad (7)$$

where $T_{ij}(\boldsymbol{y},\omega)$ is the Lighthill's tensor related to the volumic sources, $\hat{Q}_n(\boldsymbol{y},\omega)$ and $\hat{F}_i(\boldsymbol{y},\omega)$ are the Fourier transform of:

$$\begin{aligned} Q_n &= (\rho u_i - \rho_\infty \overline{u}_i)n_i && \text{related to the monopolar term and} \\ F_i &= (p\delta_{ij} + \rho(u_i - 2\overline{u}_i)u_j + \rho_\infty \overline{u}_i \overline{u}_j)n_j && \text{related to the dipolar term.} \end{aligned}$$

In the following work, these integral calculations are performed using the parallelized ONERA solver *MIA* developed by G. Reboul.

IV.D. Validation cases

IV.D.1. Single harmonic gust interacting with a 2D flat-plate

The case of a single gust interacting with a flat plate with no thickness is of particular interest, because an exact solution derived by Amiet[4,5] is available. It can be adapted to 2D problems as done by Reboul.[50] Such a 2D case is useful to highlight specific behaviors such as the non-compactness effects on the acoustic response for high frequencies. The single gust is defined by a streamwise wavenumber k_x , and the amplitude is chosen to satisfy the linearity assumptions (Golubev[9] has shown that for high amplitudes gusts, non-linear effects may give rise to harmonics in the acoustic response). The incident perturbation field considered is of the form:

$$\begin{aligned} u'(\boldsymbol{x},t) &= 0 \\ w'(\boldsymbol{x},t) &= \varepsilon U_0 \cos\left(k_x(x - U_0 t)\right) \end{aligned} \quad (8)$$

where $c = 1.0$ m is the chord of the flat plate, $\varepsilon = 0.02$ is the gust intensity relative to the mean flow U_0 with a Mach number set to M=0.5. The grids designed for these validation cases are clustered at the leading and trailing edges in order to resolve the abrupt transition effects and to well capture the pressure peak at the leading edge. The grids extend until at least 6 chords around the airfoil and ensure at least 10 points per wavelength for the reduced wavenumbers $k_x^* = 1.0$, 3.0, 5.0, 10.0.

In order to speed up the removal of transients from the domain induced at the beginning of the calculations (before reaching the periodic state), the fluctuating field given by Eq. (8) is initialized over the entire domain.

Fig. 22 shows snapshots of the upwash velocity (left) and pressure (right) fluctuations for the $k_x^* = 1.0$ (top) and $k_x^* = 5.0$ (bottom) wavenumbers. As expected for gust-airfoil interaction mechanism the radiated field is dipolar and symmetric, for this particular case of a flat plate. The visible change in the pattern of the radiated field between $k_x = 1.0^*$ and $k_x = 5.0^*$ is due to the loss of compactness at high frequency. Fig. 23 shows the RMS pressure on the suction side of the plate and Fig. 24 presents the directivity for an observer distance of 4 chords around the center of the airfoil. As the acoustic responses are symmetrical, only the upper half is represented. The computational results are in good agreement with Amiet's solution and fairly well predicts the growing number of lobes due to the loss of compactness as the frequency increases. The discrepancies observed for the highest wavenumber might be lowered if using a more refined mesh.

IV.D.2. HIT interacting with a 2D flat plate

The previous 2D flat plate cases with single gust are now extended to the computation of a synthetic turbulence described by Eq. (5). The finest mesh is considered and the axial mean flow Mach number is set to M=0.5. Modes are injected between $k_{min}^* = 1.0$ and $k_{max}^* = 10.0$ with $\Delta k^* = 0.2$. The 1D von Karman spectrum is defined by $\Lambda = 0.18$ m and $T_I = 4.56.10^{-3}$.

Snapshots of velocity and pressure disturbances computed by CAA are plotted in Fig. 25, still showing the symmetric dipole pattern but with a broadband nature. Fig. 26 presents the power spectral density (PSD) directly assessed from *sAbrinA.v0* for an observer located at 4 chords above the centre of the airfoil and compared to Amiet's solution. Note that present Amiet's solution is strictly exact including the near-field term contribution (no far-field assumptions are used). A very good agreement is found between the numerical and the analytical predictions.

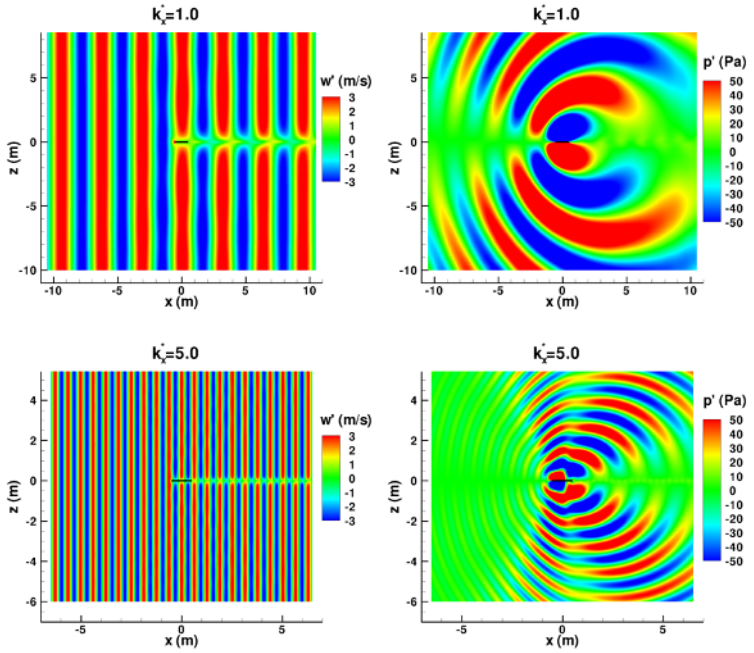

Figure 22. Upwash velocity component (left) and fluctuating pressure field (right).

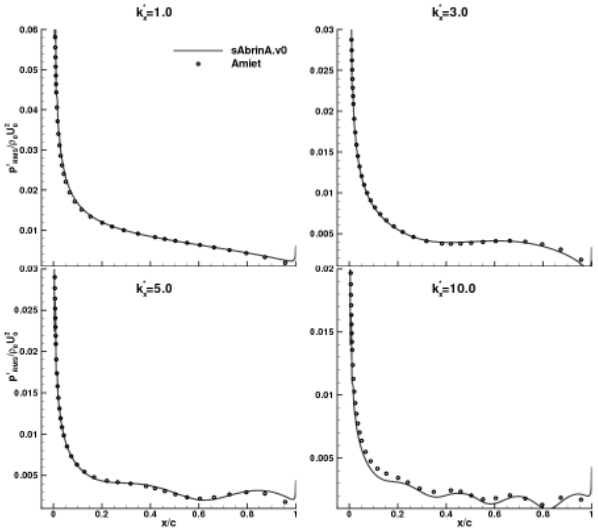

Figure 23. RMS wall pressure for single gust cases.

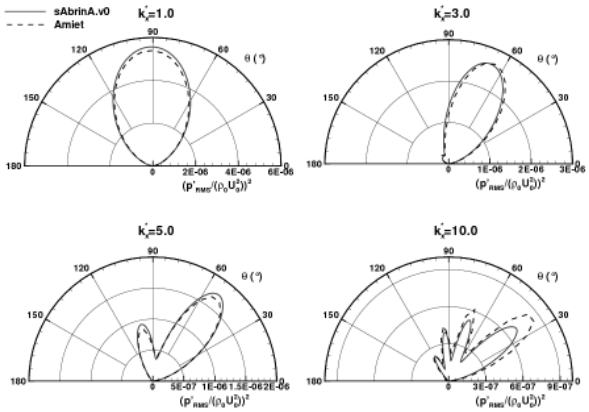

Figure 24. Directivities at 4 chords for single gust cases.

IV.D.3. 3D flat plate computation and coupling with FWH integral method

The CAA computations are extended in 3D and validated again on a flat plate case. The acoustic predictions issued from the coupling with the FWH integral described in section IV.C are presented and discussed. In order to get a reasonable CAA grid size, 3D computations are practically performed by restricting the full span L_{span} to a spanwise strip with length L_{sim} and imposing periodicty conditions at each side. This implies to choose wavelengths of spanwise wavenumbers k_y to be multiples of the simulated span ($k_{y,n} = n2\pi/L_{sim}$) so that the two-wavenumber spectrum is discretized using a spanwise wavenumber step $\Delta k_y = 2\pi/L_{sim}$. It appears that the suited spanwise extent required to ensure a significant part of the spectrum related to the most energetic values of k_y is still demanding heavy mesh size (about 100 Million points), involving quite expensive calculations. As done in ref. [46], a simplification is proposed to avoid this problem.

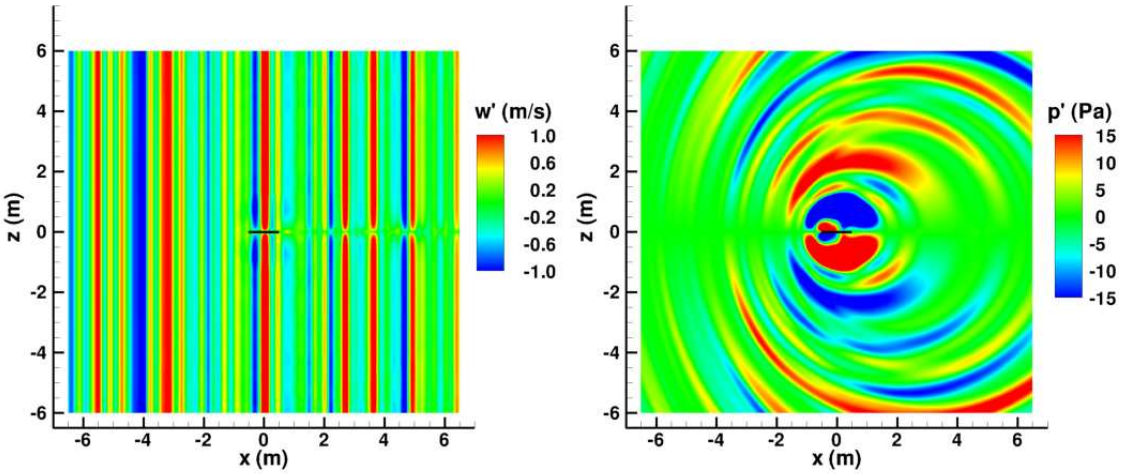

Figure 25. Upwash velocity component (left) and fluctuating pressure field (right).

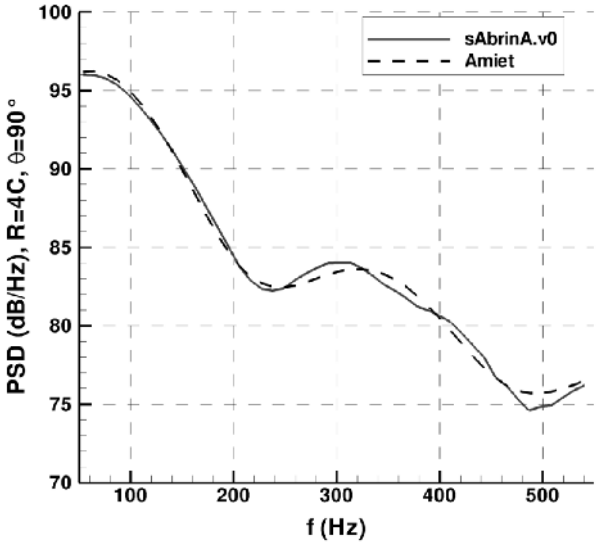

Figure 26. PSD at 4 chords and 90°.

Amiet argued that for a far-field observer in the mid-span plane of an infinite flat-plate (practically, when the span to chord ratio is greater or equal to 3), the parallel gusts ($k_y = 0$) are mainly contributing to the radiated noise. Indeed it can be shown that the contribution of cut-on oblique gusts corresponding to $k_y < k_x M/\sqrt{1-M^2}$ cancel out for a far-field observer located in the mid-span plane. This effect is highlighted in Fig. 27, in which Amiet calculations are performed for two observers located respectively at 8 chords and 65 chords above a flate plate (with a span to chord ratio of 3), by using the complete spectrum $\Phi_{ww}(k_x, k_y)$ or the zero-spanwise wavenumber spectrum $\Phi_{ww}(k_x, 0)$. As for the 2D case, the 3D Amiet solutions are obtained without far-field approximations. They are derived from a numerical integration of the response of the flat-plate using analytical aerodynamic functions.[50] Thus, an exact acoustic response with full compactness effects can be assessed. At 8 chords (Fig. 27, left) discrepancies are visible between the two calculations with and without oblique gusts contribution because the observer is not far enough from the airfoil, but at 65 chords (Fig. 27, right) the two results become identical.

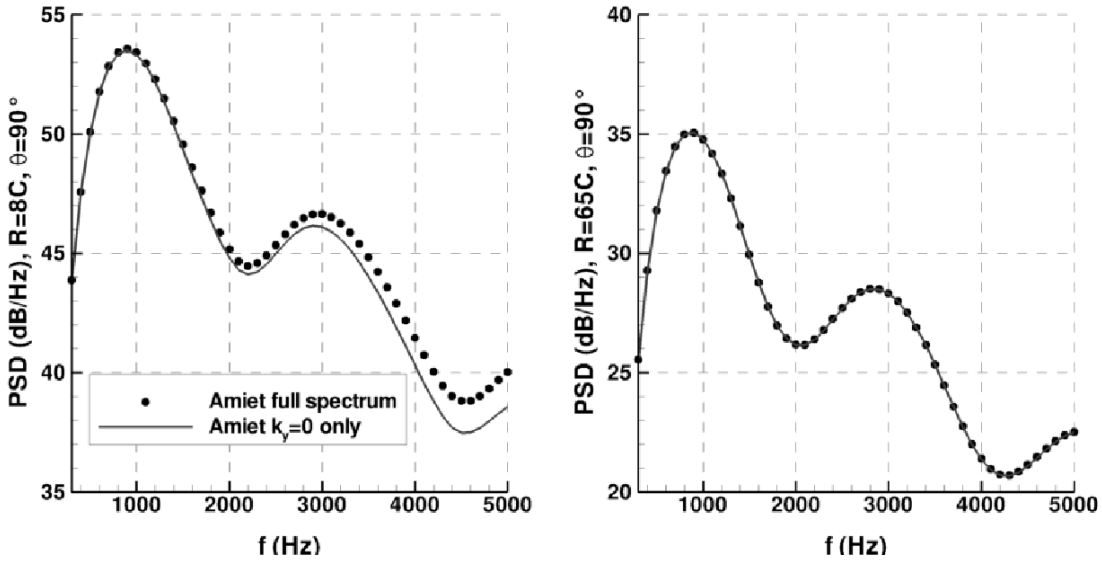

Figure 27. PSD issued from Amiet calculations at 8 chords and 65 chords above a flate plate.

Taking advantage from these conditions, only the parallel gusts can be considered in Eq. (4) when injected in the CAA (if the span to chord ratio assumptions are satisfied), which allows us to use a very limited spanwise extent. However, when using the zero-spanwise wavenumber spectrum $\Phi_{ww}(k_x, 0)$, explicit values of Δk_y are no more defined. In Amiet's theory, 3D non-compact and 2D compact formulations, respectively related to the overall spectrum $\Phi_{ww}(k_x, k_y)$ and to the parallel gusts spectrum $\Phi_{ww}(k_x, 0)$, give rise to a $2\pi/L_{span}$ factor when calculating the far-field PSD. This factor has to be included in the CAA in order to get the correct aerodynamic response of the full span airfoil. This is done by setting $\Delta k_y = 2\pi/L_{span}$ in Eq. 4.

To check this scaling factor, we consider a flat-plate with $c = 0.15$ m and $L_{span} = 0.45$ m, and a uniform mean flow $U_0 = 60$ m/s. The von Karman spectrum is defined with $\Lambda = 6$ mm and $T_I = 0.025$. These parameters are similar to the FLOCON application case presented in section V. The incoming synthetic turbulence defined by Eq. (4) is restricted to parallel gusts with wavenumbers corresponding to a maximum frequency $f_{max} = 5000$ Hz and a frequency spacing $\Delta f = 100$ Hz. The CAA strip is set equal to $L_{sim} = 10$ mm. Note that in order to take into account for compactness effects, the input are duplicated in the spanwise direction over the full span L_{span} before calculating the FWH integral given by Eq. (6).

A snapshot of the fluctuating pressure issued from the direct CAA computation in the mid-span plane is shown in Fig. 28. A comparison of the RMS wall pressure distributions issued from CAA and Amiet-based response is plotted in Fig. 29 showing a perfect agreement. The results for a 90° observer point located in the mid-span plane at 1.2 m are compared in Fig. 30. The computed PSD provided by CAA-FWH is close to the Amiet solutions obtained with and without including the oblique gusts. The oscillations observed in the numerical results might be partially explained by the pressure peak near the trailing edge (Fig. 29) which is not present in the analytical solution. The presence of this peak is explained by the abrupt change in the boundary condition at the trailing edge. Another FWH integration has been realized in removing a small part of the plate around the trailing edge (approximately 3.5% of the chord length) to investigate the effect of this peak on the radiated field. The resulting PSD is plotted in Fig. 30 and shows a slight reduction of the oscillations, particularly at high frequencies. There are still some oscillations remaining but the numerical solution is quite satisfactory.

In order to assess the flat plate response to oblique gusts without performing a heavy CAA computation on a large spanwise extent, a semi-analytical method has been set up. It consists in calculating the pressure jump on the flat plate using Amiet's aerodynamic function $g(x, k_x, k_y)$, and using it as an input to the FWH

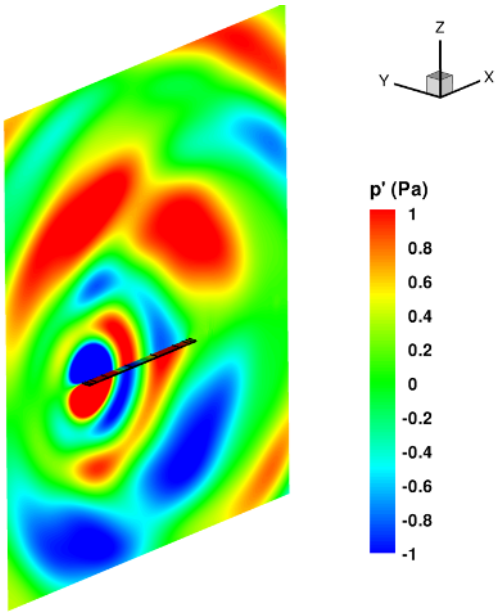

Figure 28. Snapshot of the pressure disturbance in the mid-span plane.

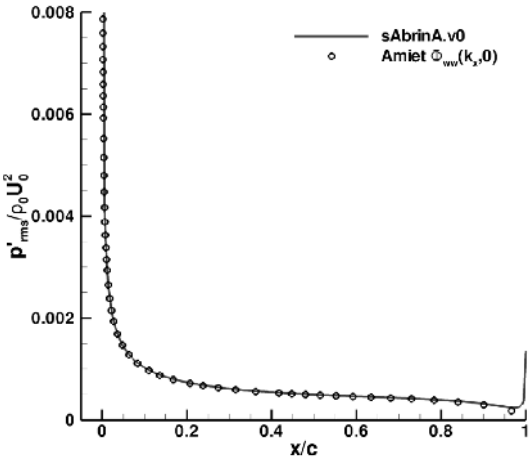

Figure 29. RMS wall pressure for the 3D flat plate.

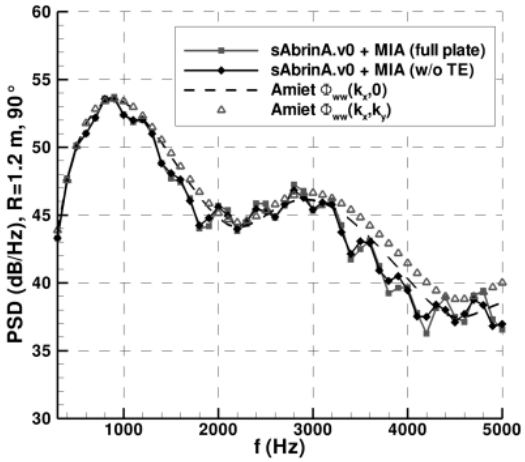

Figure 30. Predicted PSD at Robs=1.2 m and 90°.

solver MIA. The pressure jump is calculated as follows in the time domain:

$$\Delta p(x,y,t) = 2\pi\rho_0 U_0 \sum_{i=1}^{N}\sum_{j=-M}^{M} 2\sqrt{\Phi_{ww}(k_{x,i},k_{y,j})\Delta k_x \Delta k_y}\, g(x,k_{x,i},k_{y,j}) e^{i(k_{x,i}U_0 t - k_{y,j}y + \varphi_{ij})} \tag{9}$$

Or in the frequency domain:

$$\Delta\hat{p}(x,y,\omega) = 2\pi\rho_0 U_0 \sum_{j=-M}^{M} 2\sqrt{\Phi_{ww}\left(\frac{\omega}{U_0},k_{y,j}\right)\Delta k_x \Delta k_y}\, g\left(x,\frac{\omega}{U_0},k_{y,j}\right) e^{i(-k_{y,j}y+\varphi_j)} \tag{10}$$

When using the time formulation (Eq. (9)), only the real part of the pressure jump so calculated is considered as an input for the integral method. The discretization of the flat plate for these semi-analytical

computations is shown in Fig. 31. The RMS pressure distributions over the surface are plotted in Fig. 32 (right) and compared to a theoretical uniform distribution (Fig. 32, left). We can observe a quasi-uniform distribution in the spanwise direction (as expected), which makes this synthetic turbulent inflow modelled by Eq. (9) reliable in terms of energy distribution.

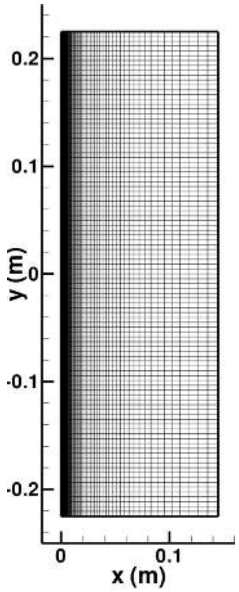

Figure 31. Flat plate mesh.

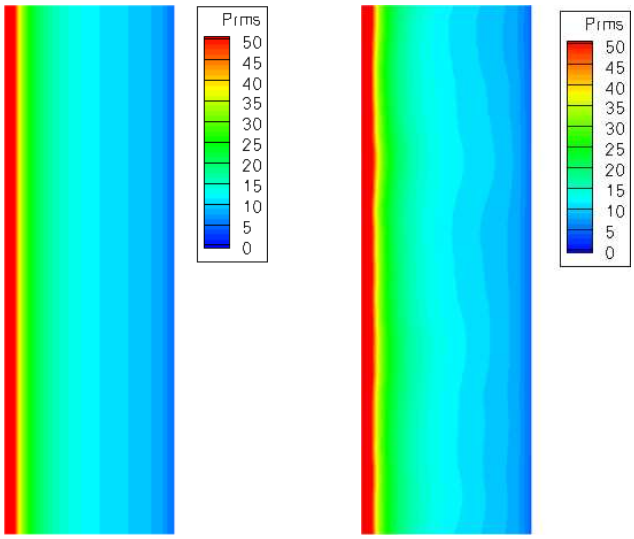

Figure 32. RMS surface pressure issued from theory (left) and computation (right).

However, the far-field PSD issued from *MIA* shown in Fig. 33 (left) is found to be quite chaotic compared to Amiet's solution. This is due to cancellation effects between spanwise waves related to the same streamwise wavenumber (i.e., the same frequency). To reduce these statistical deviations, two averaging processes are suggested. The standard one is to perform a quadratic averaging over several independent computations. The second one is to realize a single run with a smaller frequency spacing and then to smooth the spectrum by integrating the levels over consecutive frequency bands Δf. This second approach is almost equivalent as performing a periodogram for a time domain calculation as done by Gabard in ref. [51]. Both methods are applied in Fig. 33 (right), using 10 computations for the first one, and using a 10-times smaller frequency spacing and integrating over 10 bands for the second. The predictions are highly improved by the averaging.

The second approach provides a fairly good prediction and has the advantage of having to perform only one computation.

First attempts of injecting a turbulent perturbation in a CAA computation using the complete spectrum $\Phi_{ww}(k_x, k_y)$ underlined another difficulty. When dicretizing the spectrum over streamwise and spanwise wavenumbers, the number of modes to sum in order to generate the incoming perturbation in Eq. (4) become very important and then the computation of the right side in Eq. (3) appears to be a major CPU time consumer. The load balancing is not constant over the processors, leading to a high increase of the computational cost. This effect added to the requirement of a longer simulation duration are still challenging and a specific effort has to be done to improve the efficiency of this source term generation in Tam's inflow condition. For this reason, CAA computations applied to FLOCON configurations and presented in the next section are performed using $\Phi_{ww}(k_x, 0)$.

V. Application to FLOCON configurations

The methodology presented in section IV is now applied to try to assess the acoustic performance of the leading edge serractions presented in section III.C. It is applied to the baseline configuration and to the treated aifoil 2S ($A_s = 10$ mm and $\lambda_s = 10$ mm). The mean flow is assumed to be uniform everywhere in the domain ($U_0 = 60$ m/s). The effects of considering a realistic mean flow coming from a RANS calculation and

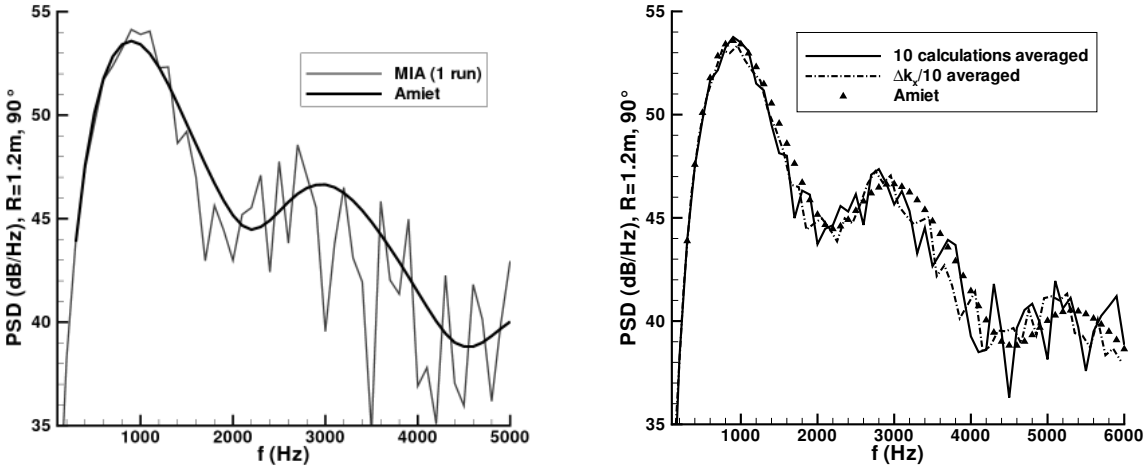

Figure 33. Predicted PSD at 90° and $R_{obs} = 1.2$ m using oblique gusts: without averaging (left) and with averaging over 10 calculations or over 10 frequency bands for 1 calculation with $\Delta f/10$ (right).

the difficulties it raises are investigated in Appendix. Considering only the parallel gusts, the CAA domain can be restricted to 10 mm in the spanwise direction (as done in the 3D flat plate case in section IV.D.3). The incident turbulent velocity field injected in the computational domain is the same than in section IV.D.3, the von Karman spectrum parameters ($\Lambda = 6$ mm and $T_I = 0.025$) are deduced from the ISVR measurements.

V.A. Baseline configuration

The computational domain is 10 mm wide in the spanwise direction ($1/45^{th}$ of the full span extent) representing approximately 7% of the chord length. This spanwise extent is similar to the one chosen for the serrated airfoil (section V.B) and is equal to the wavelength of the serration to allow the use of periodicty conditions in the spanwise direction. The mesh size is approximately 8.5 millions grid points and a CPU time of around 120 hours on 256 SGI Altix processors is required to get a fully converged solution. The grid is designed to support injected gusts up to 5 kHz, and the simulation duration (once convergence is achieved) has to be at least equal to 10 ms to ensure a frequency resolution $\Delta f = 100$ Hz. As for the flat plate case, the extracted unsteady data are duplicated in the spanwise direction (to reach the actual 0.45 m span). The PSD computed by CAA+FWH for the baseline configuration and for an observation point at 90° and 1.2 m over the airfoil (corresponding to a microphone position in ISVR test rig) is presented in Fig. 34. It is compared to the experiment and to Amiet solution.

Despite a noticeable deviation on the peak level for low frequencies behind 1 kHz, the agreement is quite satisfactory. The high levels on the measured low-frequency spectrum might be partially attributed to the background jet noise which influence is noticeable up to 1 kHz at 60 m/s as discussed in ref. [27]. The numerical predictions are very close to the Amiet solution at 90° which is consistent with preliminary 2D computational results.[3] The noticeable difference on the attenuation slope between the CAA and the measured spectra may be explained by the use of a uniform mean flow in the CAA computation, as discussed in appendix, related to the effect of a realistic mean flow around the airfoil (issued from a RANS calculation). Fig. 35 presents the OASPL calculated over frequencies between 1000 Hz and 5000 Hz in order to discard the low-frequency peak in the experimental data which would lead to an underestimation of the predicted levels. The OASPL levels of the CAA and Amiet solutions are rather close to the experiment. A slight difference between CAA and Amiet directivity patterns is attributed to the geometry of the airfoil which seems to increase the radiated noise in the front arc, and to decrease it in the rear arc.

V.B. Serrated airfoil response to parallel gusts

The serrated airfoil configuration requires a finer discretization in the spanwise direction, leading to a mesh of about 13.3 millions points. The CPU time is around 300 hours on 256 processors. A partial view of the

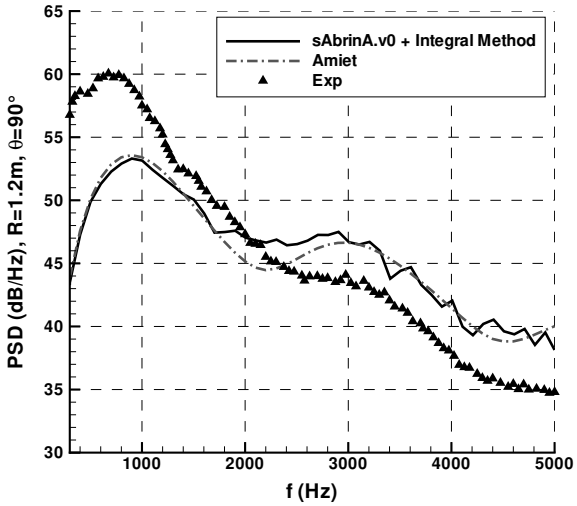

Figure 34. PSD at $R_{obs} = 1.2$ m and 90° for the baseline case.

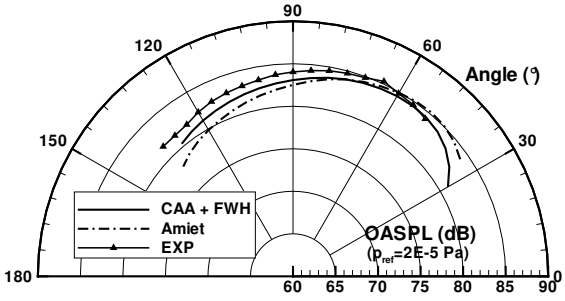

Figure 35. OASPL between 1 and 5 kHz at $R_{obs} = 1.2$ m for the baseline case.

CAA grid is shown in Fig. 36. As mentionned before, the 10 mm spanwise extent is equal to the serration wavelength ($L_{sim} = \lambda_s$), so that periodicity conditions can be applied.

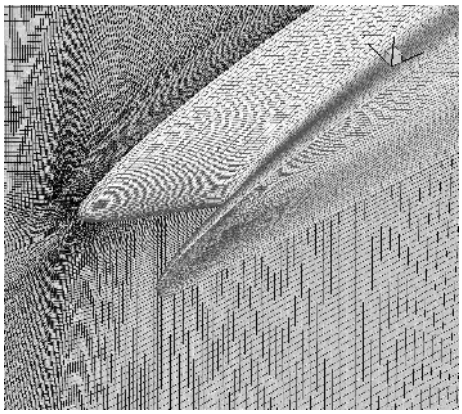

Figure 36. Partial view of the CAA mesh for the serrated wing.

A comparison between baseline and serrated cases in terms of RMS pressure fluctuation over the airfoil surface and along the chord are proposed in Figs 37 and 38, respectively. The serration effect is clearly highlighted in Fig. 37, revealing significant reductions of the levels at the top and slopes of the wave. This is addressed more precisely in Fig. 38, showing that the pressure peak at the leading edge at the root of the serration is slightly amplified compared to the baseline configuration, whereas it is reduced by more than a half at the top and at mid-slope. As the RMS surface pressure is a good indicator of the interaction noise radiated by an airfoil (especially the leading edge peak), significant reductions are expected from these observations.

Fig. 39 shows a PSD comparison between the baseline and the serrated configurations issued from the experiments (left) and the simulations (right). Quite similar trends are visible between the measurements and the numerical predictions with very close level reductions up to 3.5 kHz (see Fig. 40). This is a very promising result regarding to the complexity of the physics and the simplifications adopted in the present method. Beyond 3.5 kHz, the PWL attenuation due to the serrations is over-estimated by the simulations. This might be due to the fact that the contribution of oblique gusts ($k_y \neq 0$) not taken into account here, is no more negligible at these frequencies (contrary to the straight leading edge case), as discussed in section II. As a consequence, it could tend to balance the overall level since the spanwise gusts are getting more

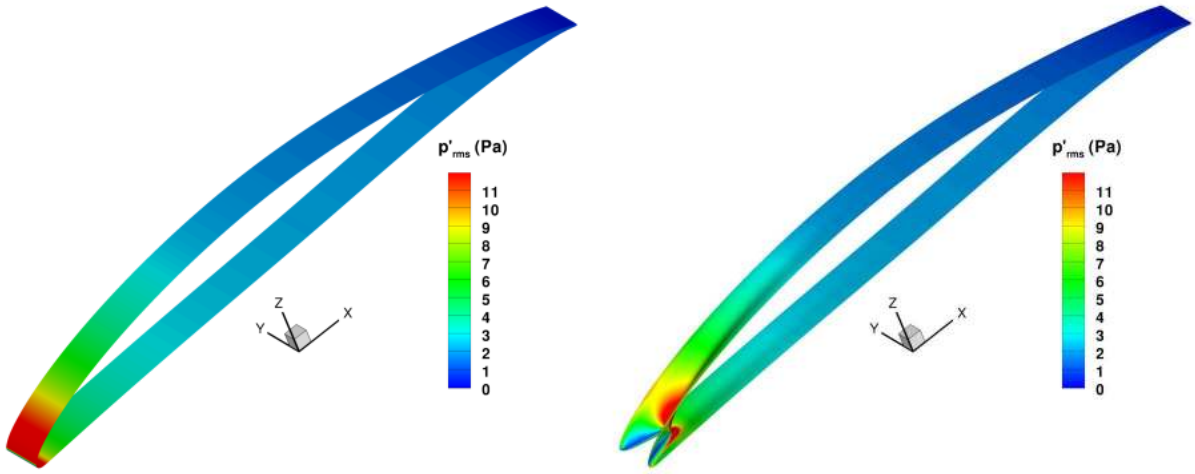

Figure 37. RMS surface pressure issued from CAA on baseline (left) and serrated (right) cases.

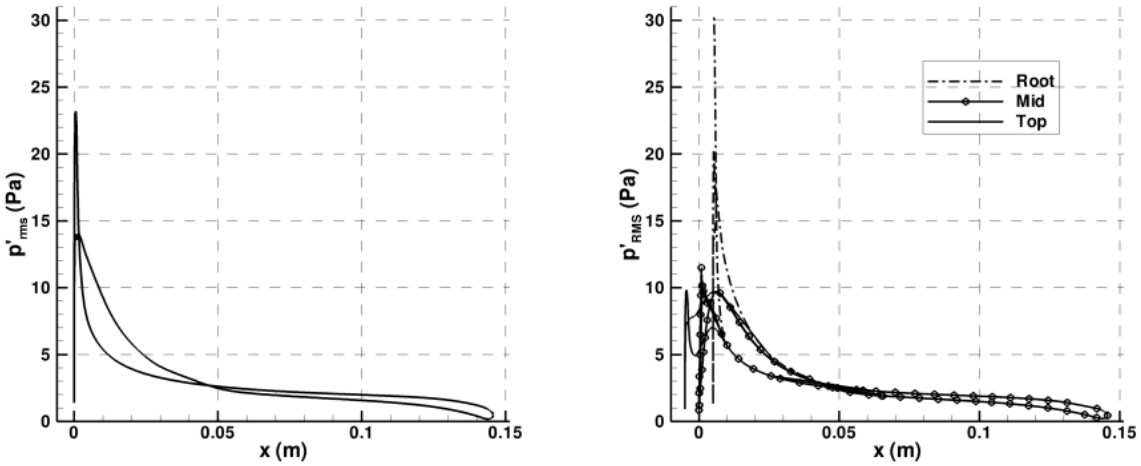

Figure 38. CAA chordwise RMS pressure profile on baseline (left) and serrated (right) cases.

and more cut-on at higher frequencies.

VI. Conclusion

In the FLOCON project, devoted to turbofan broadband noise reduction, a concept of sinusoidal leading edge serrations has been proposed by ONERA and investigated in ISVR test facility. The treatment has been tested in a dedicated isolated airfoil configuration using turbulence grid located upstream of the wing. The experimental results showed significant noise reductions on a wide frequency range for all studied flow speeds. A numerical methodology aiming at predicting turbulence interaction noise on 3D airfoil geometries (including serrations) has been presented and applied to FLOCON configurations. It is based on a CAA code solving the nonlinear Euler equations applied to the disturbances and a synthetic turbulence model fitting a prescribed HIT spectrum. The turbulent velocity field is injected at the inflow of the computational domain by means of Tam's inflow boundary condition. The method has been firstly validated on

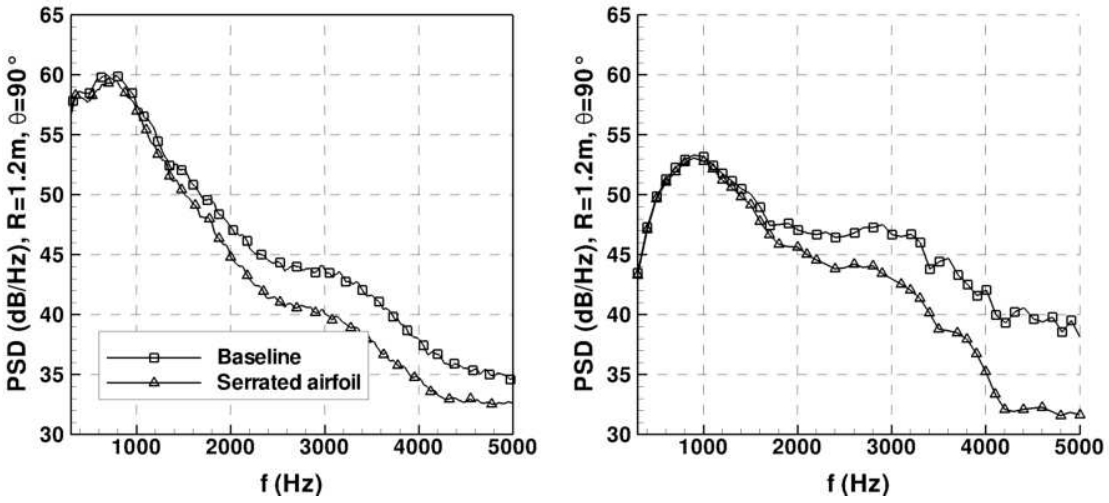

Figure 39. PSD comparison between baseline and serrated airfoils. Experiment (left) and CAA (right).

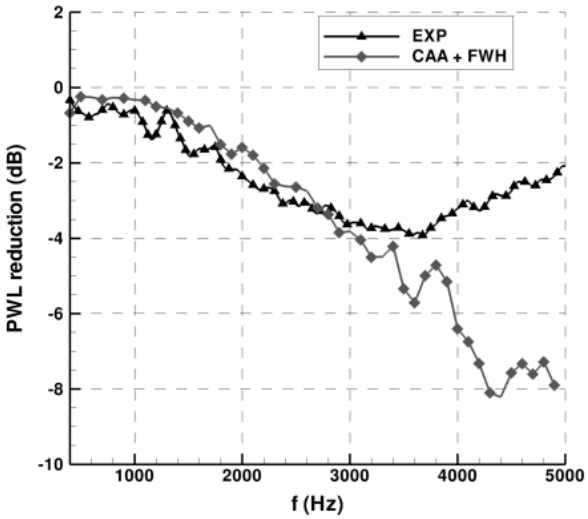

Figure 40. PWL attenuation due to the leading edge serrations.

two dimensional cases against analytical results. The coupling with an integral method solver has been validated for a three dimensional flat-plate and considering only parallel gusts. The method has then been applied to estimate the acoustic response of an isolated NACA651210 airfoil and the effect of sinusoidal leading edge serrations designed by ONERA, assuming a uniform mean flow. The acoustic spectra and noise reduction experimentally achieved have been fairly well reproduced even if an overestimation of the acoustic performances of the serrations at high frequency (beyond 3-4 kHz) has been observed and should be attributed to the spanwise gusts contribution neglected in the present computations. A basic theoretical analysis related to the spatial filtering of the gusts in the wavenumber space has been proposed to argue this point. Comparisons with computation using a RANS flow have pointed out that a uniform mean flow induces a deviation on the slope of the acoustic spectra. Nevertheless, it allows the use of a reduced grid extent and the results are free from hydrodynamic instabilities in the vicinity of the airfoil which polute the acoustic radiation. Also, when comparing to the measurements, a strong under-estimation in low frequencies (below 1 kHz) has been observed with all the employed methodologies and might certainly be attributed to installation effects. The next step of this study should be the realisation of a complementary simulation on the serrated airfoil including oblique gusts, involving a larger spanwise extent, but resulting to a huge mesh

and a much hifher CPU time. Preliminary work to speed-up the computation of the source term at the inflow when using a two-wavenumbers spectrum has to be done, as it becomes a major CPU time consumer in the CAA. A numerical study consisting in varying the parameters of the serrations and of the flow should provide a better understanding of the noise reduction mechanisms, and may allow to emerge design rules for the serrations. The present methodology will also be extended to an annular cascade configuration in order to assess the solutions proposed in a CAA benchmark[52] limited to harmonic gusts. Then the interaction between a HIT and a cascade in an annular duct[53] will be numerically investigated, in order to finally apply the methodology to realistic rotor/stator broadband noise problems by chaining the CAA to RANS or LES rotor wake computations.

Appendix: Effect of a realistic mean flow on the radiated noise

In order to study the effect of a non-uniform flow on the radiated noise, a calculation has been performed on the baseline configuration, using a RANS solution as the mean flow. For the RANS calculation, the airfoil is immersed in a free-field with an upcoming speed $U_0 = 60$ m/s ($Re \simeq 600000$). The CAA mesh for this calculation has been widen in the axial and vertical directions compared to the mesh used in section V.A, in order to move the exit boundary conditions away from the sheared regions, and then to avoid instabilities to appear and to spread near them. The new grid is more suited to data extraction over a porous surface where the mean flow is quasi-uniform, so that the use of the convected Green's function in the FWH integration is justified. The axial velocity of the mean flow solution interpolated on the CAA computational domain is presented in Fig. 41. The black line surrounding the airfoil represents the extraction surface defined for the FWH (porous surface) calculations. Fig. 42 shows a snapshot of the fluctuating pressure in the mid-span plane of the computational domain. We can observe the typical dipolar pattern emitted from the leading edge and due to turbulence-airfoil interaction. However, when the gusts are passing through the sheared flow in the vicinity of the airfoil, they trigger hydrodynamic instabilities that are convected along the airfoil surface and in its wake. These hydrodynamic modes are responsible for the pressure spots visible along the airfoil surface, that are amplified when passing through the trailing edge. Figure 43 shows the RMS wall pressure plots over the surface and along the chord. Even if the leading edge peak is modified by the RANS mean flow in comparison with the uniform flow calculation, it is still dominant. But we can also observe very strong pressure peaks near the trailing edge due to these hydrodynamic modes. These effects are similar to those resulting from the LES approach.[23] It has to be noted that in the CAA computation, a sponge layer has been set near the downstream boundary in order to dissipate the wake hydrodynamic instabilities before impacting the outside boundary of the mesh and so, to avoid possible numerical reflections.

The PSD at 1.2 m above the airfoil issued from solid and porous FWH integrations with the RANS mean flow are compared to the uniform flow solution and to the experiment in Fig. 44. The PSD computed from the calculation using a RANS mean flow are much more oscillating than the one issued from the uniform flow calculation. In order to smooth the spectra, an averaging over 5 consecutive frequency bands has been realized. The main effect of using a realistic mean flow is the noticeable increase of the decay slope which becomes closer to the experimental one, compared to the uniform flow results. As this increase of the decay slope is already visible on the solid surface results (that does not take the non-uniformity of the mean flow into account for the propagation), it tends to show that the sheared mean flow has not only an effect on the propagation of the acoustic waves, but also a strong effect in distorting the incoming velocity field in the vicinity of the airfoil which modifies the airfoils response in term of pressure distribution. The solid surface integration also shows a rise of the levels for frequencies above 5 kHz whereas no velocity modes are injected anymore. This high frequency contributions can be attributed to the trailing edge pressure peaks (highlighted in Fig. 43) since they vanish when the solid FWH integration is performed in removing the trailing edge region. This effect of the trailing edge is due to the impact of the convected hydrodynamic modes and can not be interpreted as proper self noise in this calculation since the Euler code does not solve the turbulent boundary layer developing along the airfoil.

The porous surface FWH method provides a better appraisal of the low-frequency peak and the decay slope is slightly increased compared to the solid surface calculation result. The hump at 3 kHz is better assessed too. This is possibly due to propagation effects between the airfoil and the extraction surface that could not be captured by the solid surface formulation. The cut-off of the high frequency contribution compared to the solid FWH integration might be due to the dissipation of the mesh and the filter, since the porous extraction surface is located quite far from the airfoil. Nevertheless, it seems that the main mechanism that

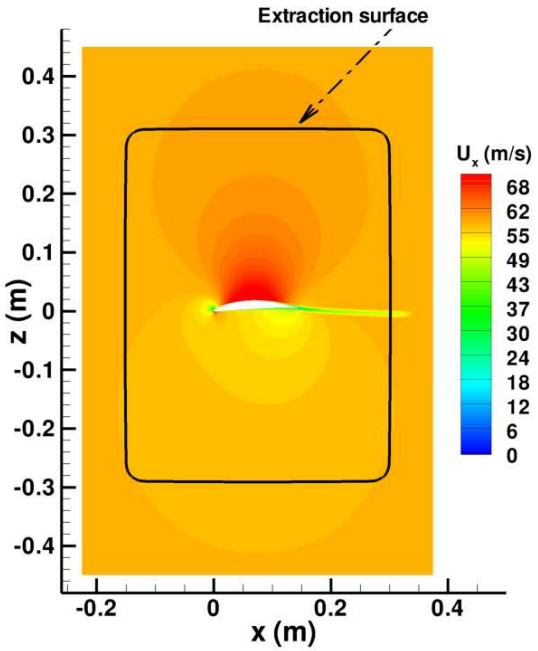

Figure 41. Axial velocity component of the RANS mean flow.

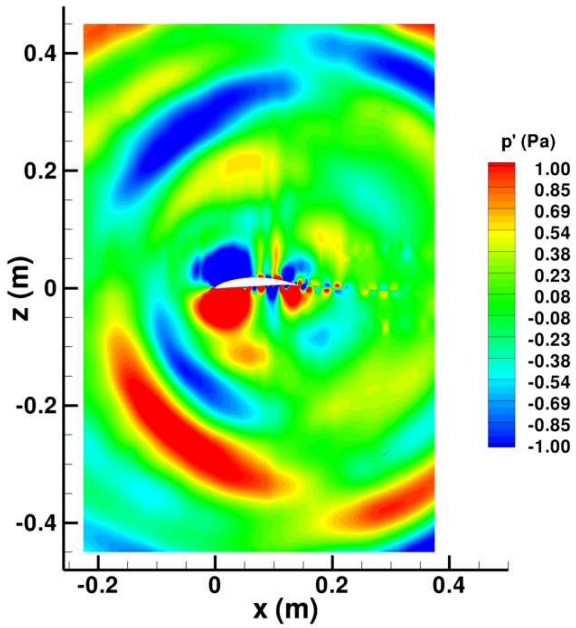

Figure 42. Snapshot of the pressure disturbance in the mid-span plane.

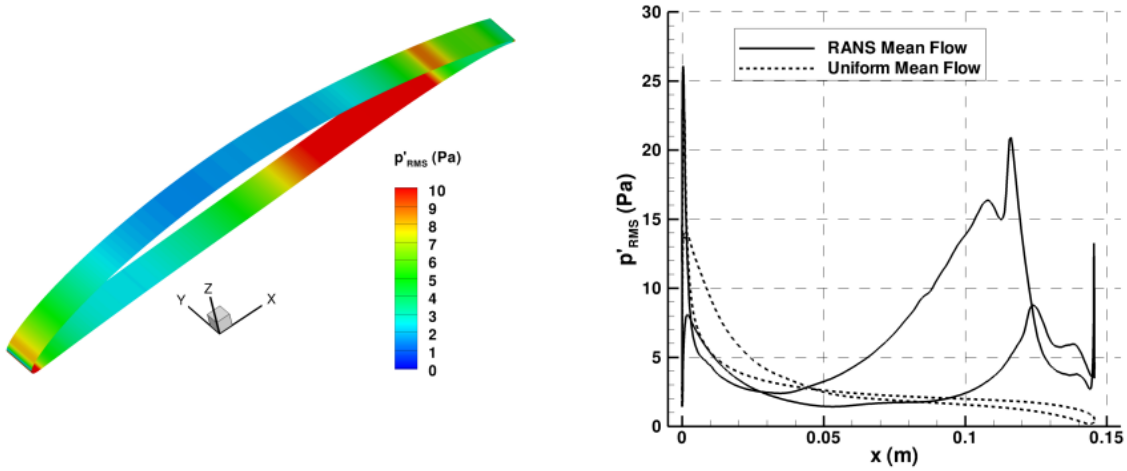

Figure 43. RMS Wall pressure for the RANS mean flow calculation over the surface (left) and along the chord.

explain the discrepancies between the uniform and the sheared mean flows solutions is the effect of the shear layer in the vicinity of the wall that distorts the incoming velocity fluctuations and modify the response of the airfoil.

Acknowledgments

This study has been supported by the European Commission (FLOCON FP7 project).

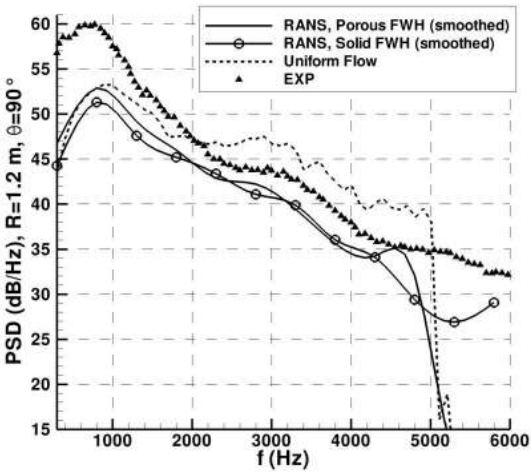

Figure 44. Comparison of the PSD between solid and porous FWH methods at $R_{obs} = 1.2$ m and 90°.

References

[1]Jacob, M.C., Boudet, J., Casalino, D., Michard, M., "A rod-airfoil experiment as benchmark for broadband noise modeling", *Theoretical and Computational Fluid Dynamics*, Vol. 19, 2005, pp.171-196.

[2]Gruber, M., "Airfoil noise reduction by edge treatments", *PhD Thesis, ISVR, University of Southampton*, 2012.

[3]Polacsek, C., Reboul, G., Clair, V., Le Garrec, T., Deniau, H., "Turbulence-airfoil interaction noise reduction using wavy leading edge : An experimental and numerical study", *Proc. of Internoise 2011*, Osaka (Japan), 2011.

[4]Amiet, R.K., "Acoustic radiation from an airfoil in a turbulent stream", *Journal of Sound Vibration*, Vol. 41, 1975, pp.407-420.

[5]Amiet, R.K., "Airfoil gust response and the sound produced by airfoil-vortex interaction", *Proc. of the 9th AIAA/NASA Aeroacoustics Conference*, AIAA Paper 84-2268, 1984.

[6]Lockard, D.P., Morris, P.J., "A parallel implementation of a computational aeroacoustic algorithm for airfoil noise", *Proc. of the 2nd AIAA/CEAS Aeroacoustics Conference*, AIAA Paper 96-1754, 1996.

[7]Lockard, D.P., Morris, P.J., "Radiated noise from airfoils in realistic mean flows", *AIAA Journal*, Vol. 36(6), 1998, pp.907-914.

[8]Scott, J.R., "Single airfoil gust response problem", *Proc. of the 4th CAA Workshop on Benchmark Problems*,NASA CP-2004-212954, 2003, pp.45-58.

[9]Golubev,V.V., Mankbadi, R.R., Scott, J.R., "Numerical inviscid analysis of nonlinear airfoil response to impinging high-intensity high-frequency gust", *Proc. of the 10th AIAA/CEAS Aeroacoustics Conference*, AIAA Paper 2004-3002, 2004.

[10]Golubev,V.V., Mankbadi, R.R., Visbal, M.R., Scott, J.R., Hixon, R., "A parametric study of nonlinear gust-airfoil interaction", *Proc. of the 12th AIAA/CEAS Aeroacoustics Conference*, AIAA Paper 2006-2426, 2006.

[11]Golubev,V.V., Mankbadi, R.R., Hixon, R., "Space-time mapping analysis of airfoil nonlinear interaction with unsteady inviscid flow", *AIAA Journal*, Vol. 43(10), 2005.

[12]Crivellini, A., Golubev,V.V., Mankbadi, R.R., Scott, J.R., Hixon, R., Povinelli, L., "Nonlinear analysis of airfoil high-intensity gust response using a high-order prefactored compact code", *Proc. of the 8th AIAA/CEAS Aeroacoustics Conference*, AIAA Paper 2002-2535, 2002.

[13]Hixon, R., Golubev, V.V., Mankbadi, R.R., Scott, J.R., Sawyer, S., Nallasamy, M., "Application of a nonlinear computational aeroacoustics code to the gust-airfoil problem", *AIAA Journal*, Vol. 44(2), 2006.

[14]Hixon, R., Sescu, A., Nallasamy, M., Sawyer, S., "Prediction of noise from realistic rotor-wake/stator-row interaction using computational aeroacoustics", *Proc. of the 15th AIAA/CEAS Aeroacoustics Conference*, AIAA Paper 2009-3339, 2009.

[15]Hixon, R., Sescu, A., Sawyer, S., "Vortical gust boundary condition for realistic rotor wake/stator interaction noise prediction using computational aeroacoustics", *Journal of Sound and Vibration*, Vol. 330, 2011, pp. 3801-3817.

[16]Ewert, R., "Broadband slat noise prediction based on CAA and stochastic sound sources from a fast random particle-mesh (RPM) method", *Computers & Fluids*, Vol. 37(4), 2008, pp.369-387.

[17]Dieste, M., Gabard, G., "Synthetic turbulence applied to broadband interaction noise", *Proc. of the 15th AIAA/CEAS Aeroacoustics Conference*, AIAA Paper 2009-3267, 2009.

[18]Dieste, M., Gabard, G., "Random-Vortex-Particle Methods for Broadband Fan Interaction Noise", *Proc. of the 16th AIAA/CEAS Aeroacoustics Conference*, AIAA Paper 2010-3885, 2010.

[19]Salem-Said, A.H., "Large eddy simulation of shear-free interaction of homogeneous turbulence with a flat-plate cascade", *PhD Thesis*, Virginia Polytechnic Institute and State University, 2007.

[20]Bechara, W., Bailly, C., Lafon,P., Candel, S.M., "Stochastic approach to noise modeling for free turbulent flows", *AIAA Journal*, Vol. 32(3), 1994, pp. 455-463.

[21]Bailly, C., Juvé, D., "A stochastic approach to compute subsonic noise using linearized Euler's equations", AIAA Paper 99-1872, 1999.

[22]Billson, M., Eriksson, L.E., Davidson, L., "Jet noise predictions using stochastic turbulence modeling", *Proc. of the 9th AIAA/CEAS Aeroacoustics Conference*, AIAA Paper 2003-3282, 2003.

[23]Deniau, H., Dufour, G., Boussuge, J.F., Polacsek, C., Moreau, S., "Affordable compressible LES of airfoil-turbulence interaction in a free jet", *Proc. of the 17th AIAA/CEAS Aeroacoustics Conference*, AIAA Paper 2011-2707, 2011.

[24]Howe, M.S., "Aerodynamic noise of a serrated trailing edge", *Journal of Fluids and Structures*, Vol. 5(1), 1991, pp.33-45.

[25]Howe, M.S., "Noise produced by a sawtooth trailing edge", *The Journal of the Acoustical Society of America*, Vol. 90(1), 1991, pp.482-487.

[26]Oerlemans, S., Fisher, M., Maeder, T., Kögler, K., "Reduction of wind turbine noise using optimized airfoils and trailing-edge serrations", *AIAA journal*, Vol. 47(6), 2009, pp.1470-1481.

[27]Gruber, M., Joseph, P., Polacsek, C., Chong, T.P., "Noise reduction using combined trailing edge and leading edge serrations in a tandem airfoil experiment", *Proc. of the 18th AIAA/CEAS Aeroacoustics Conference*, AIAA Paper 2012-2134, 2012.

[28]Soderman, P.T., "Leading-Edge Serrations Which Reduce the Noise of Low-Speed Rotors", *NASA Technical Note* D-7371, 1973.

[29]Hersh, A.S., Soderman, P.T., Hayden, R.E., "Investigation of Acoustic Effects of Leading Edge Serrations on Airfoils", *Journal of Aircraft*, Vol. 11(4), 1974, pp. 197-202.

[30]Watts, P., Fish, M., "Scalloped Wing Leading Edge", United States Patent No. 6-431-498, 2002.

[31]Miklosovic, D.S., Murray, M.M., Howle, L.E., Fish, F.E., "Leading-edge Tubercles Delay Stall on Humpback Whale (Megaptera novaeangliae) Flippers", *Physics of Fluids*, Vol. 16(5), 2004.

[32]Hansen, K.L., Kelso, R.M., Dally, B.B., "Performance Variations of Leading-Edge Tubercles for Distinct Airfoil Profiles", *AIAA journal*, Vol. 49(1), 2011, pp.185-194.

[33]Downer, L., Dockrill, P., "WhalePower Tubercle Blade Power Performance Test Report", Wind Energy Institute of Canada, 2008.

[34]Hansen, K.L., Kelso, R.M., Doolan, C.J., "Reduction of Flow Induced Tonal Noise through Leading Edge Tubercle Modifications", *Proc. of the 16th AIAA/CEAS Aeroacoustics Conference*, AIAA Paper 2010-3700, 2010.

[35]Feinermann, J., Koushik, S., Schmitz, F.H., "Effect of Leading-Edge Serrations on Helicopter Blade-Vortex Interaction Noise", *Proc. of the 67th AHS International Annual Forum*, 2011.

[36]Graham, J.M.R., "Similarity rules for thin aerofoils in non-stationary subsonic flows", *Journal of Fluid Mechanics*, Vol. 43(4), 1970, pp. 753-766.

[37]Adamczyk, J.J., "The passage of an infinite swept airfoil through an oblique gust", *NASA Contractor Report*, NASA CR-2395, 1974.

[38]Moreau, S., Henner, M., Iaccarino, G., Wang, M., "Analysis of Flow Conditions in Free-jet Experiments for Studying Airfoil Self-Noise", *AIAA journal*, Vol. 41(10), 2003, pp.1895-1905.

[39]Moreau, S., Roger, M., "Competing broadband noise mechanisms in low-speed axial fans", *AIAA journal*, Vol. 45(1), 2007, pp.48-57.

[40]Redonnet, S., Manoha, E., Sagaut, P., "Numerical simulations of propagation of small perturbations interacting with flows and solid bodies", *Proc. of the 7th AIAA/CEAS Aeroacoustics Conference*, AIAA Paper 2001-222, 2001.

[41]Polacsek, C., Burguburu, S., Redonnet, S., Terracol, M., "Simulations of fan interaction noise using a hybrid approach", *AIAA Journal*, Vol. 44(6), 2006, pp. 1188-1196.

[42]Redonnet, S., "Numerical study of acoustic installation effects with a computational aeroacoustics method", *AIAA Journal*, Vol. 48(5), 2010, pp. 929-937.

[43]Tam, C.K.W., Dong, Z., "Radiation and outflow boundary conditions for direct computation of acoustic and flow disturbances in a nonuniform mean flow", *Journal of Computational Acoustics*, Vol. 4(2), 1996, pp. 175-201.

[44]Tam, C.K.W., "Advances in numerical boundary conditions for computational aeroacoustics", *Journal of Computational Acoustics*, Vol. 6(4), 1998, pp. 377-402.

[45]Kraichnan, R.H., "Diffusion by a random velocity field", *Physics of fluids*, Vol. 13(1), 1970, pp. 22-31.

[46]Casper, J., Farassat, F., "A new time domain formulation for broadband noise predictions", *International Journal of Aeroacoustics*, Vol. 1(3), 2002, pp. 207-240.

[47]Curle, N., "The influence of solid boundaries upon aerodynamic sound", *Proceeding of the Royal Society*, Vol. 231(3), 1955, pp. 505-514.

[48]Lockard, D.P., "An efficient, two-dimensional implementationof the Ffowcs Williams and Hawkings equation", *Journal of Sound and Vibration*, Vol. 229(4), 2000, pp. 897-911.

[49]Lockard, D.P., "A comparison of Ffowcs Williams-Hawkings solvers for airframe noise applications", *Proc. of the 8th AIAA/CEAS Aeroacoustics Conference*, AIAA Paper 2002-2580, 2002.

[50]Reboul, G., "Modélisation du bruit à large bande de soufflante de turboréacteur", *PhD Thesis*, Ecole Centrale de Lyon, 2010.

[51]Gabard, G., "Stochastic sources of broadband noise for time-domain simulations of duct acoustics", *Proc. of the 18th AIAA/CEAS Aeroacoustics Conference*, AIAA Paper 2012-2239, 2012.

[52]Namba, M., Schulten, J., "Category 4-fan stator with harmonic excitation by rotor wake", *Third Computational Aeroacoustics (CAA) Workshop on Benchmark Problems*, NASA/CP-200-209790, 2000, pp. 73-86.

[53]Posson, H., Roger, M., "Experimental validation of a cascade response function for fan broadband noise predicitions", *AIAA Journal*, Vol. 49(9), 2011, pp. 1907-1918.